2010

A 3-D Monte Carlo radiative transfer model for the disk of Gamma Cassiopeiae

Stephanie R. Rety
The University of Toledo

A Thesis

entitled

A 3-D Monte Carlo Radiative Transfer Model for the Disk of Gamma Cassiopeiae

by

Stephanie R. Rety

Submitted to the Graduate Faculty as partial fulfillment of the requirements

for the Master of Science in Physics

Dr. Jon E. Bjorkman, Committee Chair

Dr. J. D. Smith, Committee Member

Dr. Rupali Chandar, Committee Member

Dr. Patricia R. Komuniecki, Dean
College of Graduate Studies

The University of Toledo
August 2010

An Abstract of

A 3-D Monte Carlo Radiative Transfer Model for the Disk of Gamma Cassiopeiae

by

Stephanie R. Rety

Submitted to the Graduate Faculty as partial fulfillment of the requirements
for the Master of Science in Physics

The University of Toledo
August 2010

We have modeled the circumstellar disk of the B0.5 IVe star γ Cassiopeiae using a 3-D non-local thermodynamic equilibrium Monte Carlo radiative transfer code. The code produces a self-consistent determination of the electron temperature, hydrogen level population, and gas density for hot star disks. We have found that a viscous decretion disk model is consistent with the overall spectral energy distribution, optical and infrared line profiles, and polarization observations. We find best fit parameters of $\dot{M} = 2.0 \times 10^{-11}\ M_{\odot}\ \mathrm{yr}^{-1}$, truncation radius $\mathrm{R_d} = 250\ \mathrm{R_{\odot}}$, and inclination $i = 30°$. Our model's predicted inclination is 25 degrees less than current interferometric observations (Tycner et al. 2006), and we find inconsistencies in the Brackett 15 line profile fit. This may be indicative of some physical mechanism not included in the model which is responsible for additional heating in the inner disk, or there may be some peculiarity in the Be star γ Cas.

Acknowledgments

First and foremost I would like to acknowledge my family. To my grandmother Barbara McMahon, my father Robert and my mother Kathleen for always supporting and encouraging my education. For all the times that, as a child, you took me outside to observe on my tiny telescope on what always seemed to be a bitter cold winter night.

To all my friends and fellow graduate students, especially Sara Rother and John Royston, for all your support.

As well as Rick Irving for his technical expertise and for keeping alfrodull running. Alex Carciofi for help and guidance in setting up and running HDUST and for providing the accompanying IDL codes.

Karen Bjorkman, not only for providing the HPOL and IRTF data, but for starting me on this path 5 years ago as an undergraduate with a certain Be star by the name of 60 Cygni.

And finally, to my advisor Jon Bjorkman, for all you have taught me, as well as the time you invested in this project. For all the enlightening discussions we've had, ranging from radiative transfer to quantum field theory. But most of all for accepting

me as a graduate student, I really enjoyed this project (and I didn't have to carry out my promise to switch from astronomy to physics).

Contents

List of Tables

List of Figures

Chapter 1

Introduction

1.1 The Be phenomena

A classical Be star is defined as a non-supergiant B star whose spectrum has or has had at some time, one or more Balmer lines in emission (see Collins 1987 for a review). The emission is produced by circumstellar material which is probably equatorial and nonspherical in nature. Emission line strength may be highly variable, with the most common emission lines being H I, He I, and Fe II. In some cases, the emission lines may vanish only to reappear years or decades later.

How can we determine that the source of the line emission is a circumstellar disk? We infer this observationally from the presence of double-peaked Hα line emission, the infrared (IR) excess, a net intrinsic polarization, and, more recently, from optical Hα interferometry which has resolved the disk (see Quirrenbach et al. 1994). Struve (1931) first proposed that double-peaked emission lines were the result of circumstellar material orbiting the star, referring to it as "a nebular ring which revolves around the star and gives rise to emission lines." This idea is the simplest explanation for

the double-peaked morphology of the line profile. Material in the circumstellar disk orbiting the star produces emission lines. However, the material on one side of the disk moves towards the observer and is blueshifted, while the material on the other side moves away from the observer and is redshifted. In the center the material is moving perpendicular to the observer (in front of the star) is not doppler shifted, and we see it in absorption. Superimposing the blue-and-redshifted emission with the absorption component produces the common double-peaked Hα emission line profile.

The spectral energy distribution(SED) of Be stars commonly displays an excess flux in the infrared region. This IR excess is produced by free-free (bremsstrahlung) emission in which a free electron is accelerated due to an interaction with an ion, but is not bound to the ion. The free-free opacity increases as λ^2, thus the opacity increases with wavelength. Consequently, the effective photospheric radius of the disk increases with wavelength producing a flux excess. Therefore, the most logical explanation for free-free emission is ionized circumstellar gas. Furthermore, it has been shown that the strength of the Hα emission correlates with the IR excess (see Chokshi & Cohen 1987), indicating that the IR excess and Hα emission are produced in the same region of the disk.

Aside from being absorbed and reemitted, photons traveling through the disk can be scattered by electrons (Thomson scattering). This scattering results in the light becoming partially linearly polarized perpendicular to the plane of the scattering medium. If we were observing an unresolved spherical source (such as a spherically symmetric wind) then the light would be scattered symmetrically around the star so the net polarization would be zero. However, Be stars display an intrinsic, and often times variable, polarization not exceeding 2 percent. This intrinsic polarization indicates that the circumstellar material is not spherically symmetric and is most

likely concentrated in an equatorial disk. Although the polarization level is variable, the position angle of the intrinsic polarization does not vary (Wood et al. 1997), which is what one would expect for an equatorial disk whose orientation remains fixed while its mass varies.

Interferometric studies suggest that the geometry of the circumstellar gas is disklike and not spherically symmetric. Interferometric imaging of the circumstellar Hα emitting region find semiminor to semimajor axial ratios to be less than 1 (Quirrenbach et al. 1997, Stee 1995, and Tycner et al. 2004, 2006). Theoretical models of electron scattering due to an optically thin axisymmetric disk predict that the polarimetric position angle will be perpendicular to the plane of the disk (Brown and McLean 1977). Quirrenbach et al. (1997) find that for the Be stars included in their study, the interferometric position angles agree remarkably well with measured intrinsic polarimetric position angles, demonstrating that the position angle is perpendicular to the interferometric major axis.

The emission line strength is not the only variable component of the double-peaked line profile. The blueshifted (V) and redshifted (R) peaks do not always have equal amplitudes. In some Be stars, the relative amplitude ratio (V/R) varies quasi-periodically with typical periods of a few years. These cyclic changes in the V/R ratio are thought to be produced by one-armed spiral density waves in the disk(see Okazaki, 1991). Spiral density waves are the result of gas in elliptical orbits which precess due to some perturbing force such as a gravitational field. Where the flow velocity drops (at apastron) a density enhancement occurs. The V/R period is given by the precession period of the orbit. For this mechanism to work the gas must be in keplerian orbit. Radiative transfer modeling of one-armed density waves has produced V/R ratios consistent with emission line profiles(Hummel & Hanuschik 1997,

Carciofi et al. 2009).

While the circumstellar disk is almost certainly a disk of material that originated from the star's atmosphere, the detailed mechanism that creates and maintains such a disk remains unclear (see Porter & Rivinius 2003). Be stars generally rotate much more rapidly than B stars, at about 70-80 % of their critical velocity (Porter 1996) . Rotation rates ($v \sin i$) are obtained from the width of photospheric absorption line profiles. However the effects of gravitational darkening can lead to a systematic underestimate of the rotation velocity (Stoeckley 1968, Townsend et al. 2004). Even after correcting for gravity darkening, Cranmer et al. (2005) conclude that Be stars still rotate less than the critical velocity. In order to produce a Keplerian disk, the mass loss from the star must be injected into the disk at the Keplerian orbital speed. Thus the observed rotation rate alone does not appear sufficient to directly produce the disk. Some additional factor, such as nonradial pulsations, binary companions or possible magnetic fields, is required in order to add the necessary angular momentum to form the disk.

Stellar winds have been observed in the UV resonance lines of Be stars (Snow 1981). Stellar winds consist of particles flowing off the star in trajectories which we can think of as streamlines. In a rapidly rotating star, the streamlines fall towards the equator as a consequence of angular momentum conservation. In the wind compressed disk model (WCD) (see Bjorkman and Cassinelli 1993), streamlines from the northern and southern hemispheres collide in the equatorial plane, leading to a shock compressed, high density region at the equator. However, the wind compressed disk model alone was not sufficient to explain observed IR excess (Porter 97), and observational evidence suggests that the disk is moving mainly azimuthally($v_\phi >> v_r$), while the WCD model produces sub-keplerian azimuthal velocities and substantial radial velocities in

the equatorial plane.

Recently, magnetic fields have been added to the wind compressed disk model. Although high mass stars do not possess convective outer envelopes common to low mass stars such as our Sun, measurements of magnetic fields with magnitudes large enough to be dynamically important do exist for several Be stars (Henrichs et al. 2000, Donati et al. 2001). Unless a star is rotating very close to the critical velocity, rotation alone has little effect on the mass loss rate. However, combining the effects of rotation with a moderate magnetic field can produce increases by several orders of magnitude in the mass loss rate, wind momentum, and wind energy.

Cassinelli et al. (2002) proposed the magnetically torqued disk (MTD) model which used a dipolar magnetic field to channel the wind towards the disk and employed the magnetic torque to supply the necessary angular momentum. Unfortunately, time-dependant numerical magnetohydrodynamic (MHD) simulations that include stellar rotation have not reproduced the results of the analytic MTD model (Owocki & ud Doula 2003). In particular, the MHD simulations produce large radial motions (both infall and outflow) in the disk which violates the observational constraint that $v_r << v_\phi$. Allowing for dissipative (viscous) effects after matter has decoupled from the magnetic field produces a larger disk which may correct for some of these discrepancies (Brown et al. 2004).

Finally, mechanisms such as non-radial pulsations and explosive events (e.g., coronal mass ejections in the stellar wind) have been proposed for adding enough energy and angular momentum to lift material off the star. Short term variations have been observed in the photospheric line profiles of Be stars that are indicative of non-radial pulsations(NRP) (Rivinius et al. 2003). Non-radial pulsations are strongest in the

equatorial region, which suggests pulsations may provide the extra force to lift the gaseous material into orbit. Furthermore it has been observed that outbursts of μ Cen occur when several pulsation modes add in phase (Rivinius et al. 1998), although an actual physical mechanism for adding the required angular momentum has yet to be proposed. "Explosive" events may eject material isotropically from the stellar photosphere (Kroll & Hanuschick 1997). Material thrown in the direction of the stellar rotation gains both energy and angular momentum, and may orbit the star, while material thrown in the retrograde direction falls back to the star almost immediately.

Regardless of the detailed physical mechanism that initially puts the material into orbit around the star, viscosity will cause orbiting material to diffuse outward. In the viscous decretion disk scenario, it is assumed that some such mechanism exits and that the disk is formed via viscous diffusion(Lee, Saio, & Osaki 1991). Therefore it is possible to produce a steady-state model of the circumstellar disk, without prior knowledge of the disk formation mechanism.

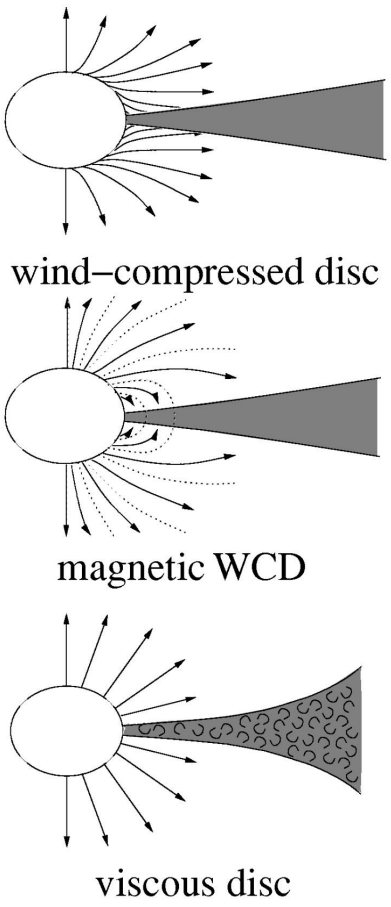

Figure 1-1: Three different models of disk formation. In the WCD model streamlines from the stellar wind are responsible for equatorial density enhancements. The MTD model channels the streamlines along the magnetic field to produce a disk. In the viscous decretion disk scenario some additional mechanism, such as non-radial pulsations or explosive events, adds angular momentum to the disk. Image from Porter and Rivinius (2003).

1.2 Gamma Cassiopeiae

In 1867, Secchi first published observations of hydrogen-beta emission from Gamma Cassiopeiae (HD 5394, HR 264, B0.5 IVe). γ Cas is often defined as being a "prototypical" Be star, although it displays unusual X-ray emission (see Smith et al. 2004). Its X-ray emission (kT $\sim 10 - 12$keV) is harder than most normal O-B stars (kT ~ 0.5keV), while the radiated luminosity is midway between that of normal stars ($\leq 10^{32}$ergs^{-1}) and classical Be+neutron star systems($\geq 10^{33}$ergs^{-1}). Harmanec et al. (2000) and Miroshnichenko et al. (2002) determined that γ Cas was most likely in a binary system with a 204-day period, where the mass of the secondary in the range of 0.5-2 $M_{\odot}$. Although the exact nature of its companion is unknown, there is some suggestion that the hard X-ray emission may be due to accretion onto a white dwarf, representing a new class of Be/xray binaries (Lopes de Oliveira et al. 2007).

There is a wide range of observational data available for γ Cas in the literature (see Telting et al. 1993), and it is one of several Be stars whose disk has been optically resolved. Combining optical Hα interferometry with polarimetry observations Quirrenbach et al. (1997) determined an inclination angle of 46°and the position angle of the major axis of the disk to be 19± 2°. Tycner et al. (2006) also performed interferometric observations of γ Cas; they found that the inclination angle was at least 55 degrees, and the position angle was $31°.2 \pm 1°.2$. Although they attribute the larger position angle value to several possibilities including intrinsic variability in the polarization of the source, residual effects associated with the removal of interstellar polarization, or a nonaxisymmetric scattering surface.

1.3 Modeling History

γ Cas is a well studied star, so unsurprisingly it has been subject to several previous modeling attempts. Early radiative transfer models of circumstellar disks in Be stars were limited by the amount of observational data available. Due to the large number of adjustable parameters, it was difficult to judge the uniqueness of the model's fits. Poeckert and Marlborough (PM, 1978) addressed this problem by fitting not only the visible, IR, and radio flux, but also the Hα and Hβ line profiles, as well as polarization in the visible and near-IR regions for γ Cas. PM obtained decent fits to the spectral energy distribution (SED), with the largest discrepancies occurring in the IR continuum fit. The polarization had the correct wavelength dependance, but was too large, and the Hβ and Hγ line profiles were too broad in the wings.

Waters, Coté &, Lamers (1987), and references therein, modeled the excess IR emission by assuming a radial power law distribution for the density of $\rho \propto r^{-n}$. By fitting the model to IR observations, the authors found values of n in the range of $2 - 3.5$, with $n = 3.25$ for γ Cas. In both the PM and Waters models the electron temperature was assumed to be isothermal throughout the disk. However, it should be noted that the spectral slope will have a dependance on the temperature gradient in the disk (Cassinelli & Hartmann 1977).

Part of this problem was addressed by Millar and Marlborough (1998) when they developed the first code to self-consistently solve for electron temperature as a function of radius within the disk. They did so by first calculating the rates of energy gain and loss due to photoionization, radiative recombination, collisional transitions between bound levels, free-free emission and free-free absorption for a set of grid points. Then by implementing radiative equilibrium within the PM model, using the "on-

the-spot approximation" to account for diffused radiation, Millar and Marlborough were able to determine the temperature structure of the disk. They then applied the code to calculate the electron temperature for several Be stars including γ Cas (Millar and Marlborough, 1999). Calculated electron temperatures were on average 2-3 times lower than the isothermal disk temperature determined by Waters(1986).

Building on the Millar and Marlborough code, Sigut and Jones(2007) modeled the temperature structure of γ Cas's disk with their code BEDISK. Sigut and Jones included heating and cooling rates from He, CNO, Mg, Si, Ca, and Fe, instead of assuming a pure hydrogen disk. Assuming a power-law equatorial gas density, they obtained a best model fit from the IR excess to be $\rho \approx$ (3-5) $\times$ $10^{-11}(r/R_*)^{-2.5}$ g cm^{-3}. In the solar composition model, the lower density envelopes generally display cooler (by 1-2000 K) density-weighted average disk temperatures than for hydrogen alone. While in higher density envelopes, absorption of ionizing radiation tended to offset the additional cooling.

One limitation of the Sigut and Jones model is that they employ 1-D annular rings to model the disk, therefore they are unable to properly account for diffuse radiation. To overcome such limitations, Carciofi and Bjorkman (2006) developed a fully 3-D radiation transfer code HDUST. HDUST employs Monte Carlo simulation methods to calculate the temperature structure of the disk, solves the steady state fluid equations for the disk, and finally calculates observable properties (see chapters 2 and 3 for a complete discussion). The purpose of this thesis is to first critically test the viscous decretion disk scenario, and then determine the physical parameters of the circumstellar disk of γ Cas. In order to accomplish this we will model UV, visible, IR, millimeter, and centimeter photometry, optical spectropolarimetry, Hα, and IR line profiles of γ Cas.

Chapter 2

Viscous Decretion Disks

Disks are a common phenomena in many astronomical objects, from protostars to accretion disks around black holes. Observations of Be star disks suggest that the gaseous material in the disk (orbiting the star) undergoes keplerian rotation, which supports the viscous decretion disk model (see introduction for discussion). In this scenario, angular momentum from some, as yet unknown, mechanism is added to stellar material, which is injected into the base of the disk. Viscosity then transports angular momentum(and matter) radially outward from the base of the disk. This process is just the reverse of what we typically think of for accretion disks, and it occurs whenever the radial density gradient is sufficiently large.

In order to determine if this scenario is correct, we must test viscous decretion model predictions against observations. The gas in the disk has keplerian motion which implies the disk is hydrostatically supported in the vertical direction, while the radial structure is determined by the viscosity. In order to produce models we must determine this structure. The vertical structure or density is governed by the scale height, which is controlled by the temperature.

2.1 Hydrostatic Structure

Since observational evidence suggests that circumstellar disks in Be stars are keplerian by nature, we can obtain a relatively simple solution to the fluid equations that determine the velocity and density of the disk. Following Bjorkman(1997), we first derive the density and velocity of the disk from the continuity and momentum equations for an orbiting gas. Using cylindrical coordinates (ϖ, ϕ, z), and assuming steady state ($\partial/\partial t = 0$), i.e. time independent, we obtain the following fluid equations:

$$\frac{1}{\varpi}\frac{\partial}{\partial \varpi}(\varpi \rho v_\varpi) + \frac{1}{\varpi}\frac{\partial}{\partial \phi}(\rho v_\phi) + \frac{\partial}{\partial z}(\rho v_z) = 0 \ , \tag{2.1}$$

$$v_\varpi \frac{\partial v_\varpi}{\partial \varpi} + \frac{v_\phi}{\varpi}\frac{\partial v_\varpi}{\partial \phi} + v_z \frac{\partial v_\varpi}{\partial z} - \frac{v_\phi^2}{\varpi} = -\frac{1}{\rho}\frac{\partial P}{\partial \varpi} + f_\varpi \ , \tag{2.2}$$

$$v_\varpi \frac{\partial v_\phi}{\partial \varpi} + \frac{v_\phi}{\varpi}\frac{\partial v_\phi}{\partial \phi} + v_z \frac{\partial v_\phi}{\partial z} + \frac{v_\varpi v_\phi}{\varpi} = -\frac{1}{\rho \varpi}\frac{\partial P}{\partial \phi} + f_\phi \ , \tag{2.3}$$

$$v_\varpi \frac{\partial v_z}{\partial \varpi} + \frac{v_\phi}{\varpi}\frac{\partial v_z}{\partial \phi} + v_z \frac{\partial v_z}{\partial z} = -\frac{1}{\rho}\frac{\partial P}{\partial z} + f_z \ . \tag{2.4}$$

Gravity is the only external force, and the central star is the primary gravitational force since $M_* >> M_{\rm disk}$. Therefore the force $\mathbf{f}$ has components:

$$f_\varpi = -\frac{GM_*\varpi}{(\varpi^2 + z^2)^{3/2}} \tag{2.5}$$

$$f_z = -\frac{GM_* z}{(\varpi^2 + z^2)^{3/2}} \tag{2.6}$$

$$f_\phi = 0 \ . \tag{2.7}$$

By making several approximations, we can greatly simplify the fluid equations. Aside from using a steady state approximation, we assume that the gas orbits the

star in a keplerian orbit, in which case v_ϖ and $v_z = 0$. The streamlines are circles of radius ϖ, where the gas moves only in the phi direction. Since $f_\phi = 0$, gravity does not exert any torques, so we conclude that our system is axisymmetric ($\partial/\partial\phi = 0$). Setting v_ϖ, v_z, $\partial/\partial\phi = 0$, the fluid eqs. (2.1)-(2.4) become:

$$\frac{1}{\rho}\frac{\partial P}{\partial \varpi} = \frac{v_\phi^2}{\varpi} + f_\varpi \tag{2.8}$$

$$\frac{1}{\rho}\frac{\partial P}{\partial z} = f_z \ , \tag{2.9}$$

and, using equations (2.2) and (2.4), we can rewrite eqs. (2.8) and (2.9) to be

$$\frac{v_\phi^2}{\varpi} = \frac{1}{\rho}\frac{\partial P}{\partial \varpi} + \frac{GM_*\varpi}{(\varpi^2+z^2)}^{3/2} \ , \tag{2.10}$$

$$\frac{1}{\rho}\frac{\partial P}{\partial z} = -\frac{GM_* z}{(\varpi^2+z^2)^{3/2}} \ . \tag{2.11}$$

In order to solve these equations, we can express them in terms of characteristic velocities. The equation of state is $P = \rho a^2$, where a is the isothermal sound speed. The escape speed is given by $V_{\rm esc}^2 = GM_*/2R$, with R being the equatorial radius of the star, and $V_{\rm crit}^2 = \frac{1}{2}V_{\rm esc}^2$. $V_{\rm crit}$ is the maximum rotation rate at the equator (the stars so called "breakup" or critical velocity). In terms of these velocities, the fluid equations become:

$$\frac{v_\phi^2}{\varpi} = \frac{1}{\rho}\frac{\partial(a^2\rho)}{\partial \varpi} + \frac{V_{crit}^2 R}{\varpi^2}\left[1+(\frac{z}{\varpi})^2\right]^{-3/2} \ , \tag{2.12}$$

$$\frac{1}{a^2\rho}\frac{\partial(a^2\rho)}{\partial z} = -\frac{V_{crit}Rz}{a^2\varpi^3}\left[1+(\frac{z}{\varpi})^2\right]^{-3/2} \ . \tag{2.13}$$

Generally $a << V_{\rm crit}$, and in the thin disk approximation $z << \varpi$ (because the radius is much larger than the scale height). From these approximations we find that for equation (2.12)

$$v_\phi = V_{crit}\sqrt{R/\varpi} \ , \tag{2.14}$$

since gravity is much larger than the pressure gradient term and $(z/\varpi)^2$ has a very small value.

In order to obtain an initial solution for the density we must solve the hydrostatic equilibrium, with the assumption that the temperature varies with ϖ, but not in the z-direction. Therefore the disk is vertically isothermal, and we can assume that a is only a function of ϖ. From equation (2.13) we find

$$\frac{a^2}{\rho}\frac{\partial \rho}{\partial z} = \frac{V_{\rm crit}^2 R z}{\varpi^3}\left[1+(\frac{z}{\varpi})^2\right]^{-3/2} \quad , \tag{2.15}$$

which we can express as:

$$\frac{1}{\rho}\frac{\partial \rho}{\partial z} = -\left(\frac{V_{\rm crit}}{a}\right)^2\left(\frac{R}{\varpi^3}\right)\frac{z}{[1+(\frac{z}{\varpi})^2]^{3/2}} \quad . \tag{2.16}$$

Then integrating from the midplane($z=0$) to an arbitrary height(z), we find

$$\rho(z,\varpi) = \rho_0(\varpi)\mathrm{e}^{-(V_{\rm crit}/a)^2\left(\frac{R}{\varpi}\right)\left[1-\frac{1}{\sqrt{1+(\frac{z}{\varpi})^2}}\right]} \quad . \tag{2.17}$$

Using the thin disk approximation ($z << \varpi$), equation (2.14), and defining the scale height as $H = (a/v_\phi)\varpi$, it can be shown that:

$$\rho(z,\varpi) \approx \rho_0(\varpi)\mathrm{e}^{-1/2(\frac{z}{H})^2} \quad . \tag{2.18}$$

In the absence of viscous effects, the value for ρ_0 is undetermined since we can place any arbitrary amount of material at a certain radius(ϖ) and it will orbit. Integrating (2.18) over z, we find the surface density

$$\Sigma = \int_{-\infty}^{\infty} \rho dz = \sqrt{2\pi} H \rho_0(\varpi) \ . \tag{2.19}$$

2.2 Vertically Nonisothermal disk structure

Initially we assumed that the disk temperature was vertically isothermal, or the disk temperature does not change with increasing height above the midplane (z). A more realistic approach is to integrate eq. (2.15) along the z-direction to obtain:

$$\rho(\varpi, z) = \rho_0(\varpi) \frac{T_0(\varpi)}{T(\varpi, z)} \exp\left[-\frac{1}{2H_0^2} \int_0^{z^2} \frac{T_0(\varpi)}{T(\varpi, z')} dz'^2 \right] \tag{2.20}$$

where

$$H_0(\varpi) = \frac{a(z=0)}{V_{\rm crit}} \varpi^{\frac{3}{2}} \ . \tag{2.21}$$

From eq. (2.19) the surface density is

$$\Sigma(\varpi) = \rho_0(\varpi) T_0(\varpi) \int_{-\infty}^{\infty} \frac{1}{T(\varpi, z)} \exp\left[-\frac{1}{2H_0^2(\varpi)} \int_0^{z^2} \frac{T_0(\varpi)}{T(\varpi, z')} dz'^2 \right] \ , \tag{2.22}$$

which can be expressed as

$$\rho_0(\varpi) = \frac{\Sigma(\varpi)}{T_0(\varpi) \int_{-\infty}^{\infty} \frac{1}{T(\varpi,z)} \exp\left[-\frac{1}{2H_0^2(\varpi)} \int_0^{z^2} \frac{T_0(\varpi)}{T(\varpi,z')} dz'^2 \right]} \ . \tag{2.23}$$

Subsituting eq. (2.23) into eq. (2.20) we can express the density as

$$\rho(\varpi, z) = \frac{\Sigma(\varpi) \exp\left[-\frac{1}{2H_0^2(\varpi)} \int_0^{z^2} \frac{T_0(\varpi)}{T(\varpi,z')} dz'^2 \right]}{T(\varpi, z) \int_{-\infty}^{\infty} \frac{dz}{T(\varpi,z)} \exp\left[-\frac{1}{2H_0^2(\varpi)} \int_0^{z^2} \frac{T_0(\varpi)}{T(\varpi,z')} dz'^2 \right]} \ . \tag{2.24}$$

2.3 Viscosity

Thus far we have assumed that the gas is merely orbiting the star in a keplerian orbit. However, for our model to be a decretion disk model, some mechanism must add angular momentum to the gas in order for it to diffuse outward (or inward if we are dealing with accretion). The most likely mechanism for this process is viscosity, although the molecular viscosity time scales are much too long. The viscous diffusion time $t = \varpi^2/\nu$, where ν is the kinematic viscosity, and ϖ is the radius of the disk, is 10^{14} years for molecular viscosity! A much more reasonable mechanism is to use eddy (turbulent) viscosity (Shakura and Sunyaev, 1973).

While molecular viscosity is the transport of momentum solely by diffusion of individual particles, turbulent viscosity is produced by eddies (vortices) in the flow, which mixes material with differing momentum. In the case of eddy viscosity, $\nu = vl$, with l being the size of the eddy, and v the velocity of the eddies. Shakura and Sunyaev assumed that the maximum size of the eddies would be H (the scale height), and that $v < a$, otherwise there would be shocks in the disk. Setting $v = \alpha a$, $0 < \alpha < 1$, where α scales the velocity, the eddy viscosity is

$$\nu = \alpha a H \ . \tag{2.25}$$

Using this prescription for the viscosity, with $H = (a/v_\phi)\varpi$ and eq. (2.14), we find the viscous time diffusion to be

$$t_{\rm diff} = \frac{V_{\rm crit}}{\alpha a^2}\sqrt{R\varpi} \tag{2.26}$$

For a Be star such as γ Cas, we find from equation (2.26) it would take eight years to build a minimum 3 stellar radii disk (assuming $\alpha = 0.1$). Such timescales are small

enough to be dynamically interesting.

2.3.1 Fluid Equations with Viscosity

Now if we want to model a decretion disk, we must add viscosity to the fluid equations. We still assume that v_z =0 (hydrostatic equilibrium), and that the disk is axisymmetric ($\partial/\partial\phi = 0$). However $v_\varpi \neq 0$, although we expect $v_\varpi << a$ unless decretion rates are horrendously large. From equation (2.1) we have the continuity equation

$$\frac{1}{\varpi}\frac{\partial}{\partial\varpi}(\varpi\rho v_\varpi) = 0 \ . \tag{2.27}$$

In order to make the fluid equations one dimensional, we integrate eq. (2.27) over ϕ and z;

$$\int_0^{2\pi} d\phi \int_{-\infty}^{\infty} dz \frac{\partial}{\partial\varpi}(\varpi\rho v_\varpi) = 0 \ , \tag{2.28}$$

which yields

$$\frac{\partial}{\partial\varpi}(2\pi\varpi\Sigma v_\varpi) = 0 \ . \tag{2.29}$$

This implies the mass loss rate in the disk, $\dot{M} = 2\pi\varpi\Sigma v_\varpi$, is constant (independent of ϖ), therefore $v_\varpi = \dot{M}/2\pi\varpi\Sigma$.

In order to add angular momentum to the system, there must be a torque ($\tau = dL/dt$) from a force perpendicular to ϖ. This force arises from the viscous shear stress. If we consider the gas with a flow velocity in the ϕ direction and a velocity shear in the ϖ direction, then the force can be obtained from the $\varpi\phi$-component of the shear stress by the tensor,

$$\Pi_{\varpi\phi} = \nu\rho\varpi\frac{\partial}{\partial\varpi}(\frac{v_\phi}{\varpi}) \ , \tag{2.30}$$

which gives

$$f_\phi = \frac{1}{\rho\varpi^2}\frac{\partial\varpi^2\Pi_{\varpi\phi}}{\partial\varpi} \ . \tag{2.31}$$

Setting $v_z = 0$, and $(\partial/\partial\phi) = 0$ the momentum equations become:

$$v_\varpi\frac{\partial v_\varpi}{\partial\varpi} - \frac{v_\phi^2}{\varpi} = -\frac{1}{\rho}\frac{\partial P}{\partial\varpi} + f_\varpi \ , \tag{2.32}$$

$$v_\varpi\frac{\partial v_\phi}{\partial\varpi} + \frac{v_\varpi v_\phi}{\varpi} = \frac{1}{\rho\varpi^2}\frac{\partial\varpi^2\Pi_{\varpi\phi}}{\partial\varpi} \ , \tag{2.33}$$

$$\frac{1}{\rho}\frac{\partial P}{\partial z} = f_z \ . \tag{2.34}$$

As long as $v_\varpi << a$, the ϖ and z momentum equations (2.33) and (2.34) are the same as before (eqns. [2.8] and [2.9]), so the solutions for the velocity and vertical density structure do not change (eqs. [2.14] and [2.24]). The ϕ momentum equation (2.34) may be rewritten as

$$\rho\varpi v_\varpi\frac{\partial(\varpi v_\phi)}{\partial\varpi} = \frac{\partial(\varpi^2\Pi_{\varpi\rho})}{\partial\varpi} \ . \tag{2.35}$$

Now integrating over ϕ and z gives

$$\dot{M}\frac{\partial(\varpi v_\phi)}{\partial\varpi} = \frac{\partial\mathcal{T}}{\partial\varpi} \ , \tag{2.36}$$

where the viscous torque

$$\mathcal{T} = \int_{-\infty}^{\infty}\varpi\Pi_{\varpi\phi}2\pi\varpi dz \tag{2.37}$$

$$= -3\pi\alpha a_0^2\int_{-\infty}^{\infty}\frac{T(\varpi,z)}{T_0(\varpi)}\rho(\varpi,z)dz \ . \tag{2.38}$$

Defining the weighted mass average temperature

$$\langle T(\varpi)\rangle \equiv \frac{\int_{-\infty}^{\infty}T(\varpi,z)\rho(\varpi,z)dz}{\int_{-\infty}^{\infty}\rho(\varpi,z)dz} = \frac{\int_{-\infty}^{\infty}T(\varpi,z)\rho(\varpi,z)dz}{\Sigma(\varpi)} \ , \tag{2.39}$$

the torque becomes

$$\mathcal{T} = \frac{-3\pi\alpha a_0^2}{T_0(\varpi)} \langle T(\varpi)\rangle \ \Sigma(\varpi) \ . \tag{2.40}$$

If we integrate (2.36) over ϖ we find

$$\mathcal{T} = \dot{M} V_{\rm crit}\sqrt{R\varpi} + \text{constant} \ . \tag{2.41}$$

The integration constant is determined by the boundary conditions($\Sigma = 0$) at the outer edge of the disk ($\varpi = \mathrm{R}_d$). Then by substituting equation (2.39) into equation (2.38) and solving for the surface density we find that

$$\Sigma(\varpi) = \frac{\mu_0 m_H \dot{M} V_{\rm crit} R^{1/2}}{3\pi k\alpha\langle T(\varpi)\rangle \varpi^{3/2}} \left[\left(\frac{R_d}{\varpi}\right)^{1/2} - 1\right] \ . \tag{2.42}$$

To summarize we now have the following expressions for the velocity and density of the disk:

$$v_\varpi = \frac{\dot{M}}{2\pi\varpi\Sigma(\varpi)} \tag{2.43}$$

$$v_\phi = V_{crit}\sqrt{\frac{R}{\varpi}} \tag{2.44}$$

$$\Sigma(\varpi) = \frac{\mu_0 m_H \dot{M} V_{\rm crit} R^{1/2}}{3\pi k\alpha\langle T(\varpi)\rangle \varpi^{3/2}} \left[\left(\frac{R_d}{\varpi}\right)^{1/2} - 1\right] \tag{2.45}$$

$$\rho(\varpi, z) = \frac{\Sigma(\varpi)\exp\left[-\frac{1}{2H_0^2(\varpi)}\int_0^{z^2}\frac{T_0(\varpi)}{T(\varpi,z')}dz'^2\right]}{T(\varpi,z)\int_{-\infty}^{\infty}\frac{dz}{T(\varpi,z)}\exp\left[-\frac{1}{2H_0^2(\varpi)}\int_0^{z^2}\frac{T_0(\varpi)}{T(\varpi,z')}dz'^2\right]} \ . \tag{2.46}$$

To solve these equations, we must know the temperature as a function of position. The temperature is determined by radiative equilibrium, so we must now solve the equations of radiative transfer in the disk.

Chapter 3

3-D NLTE Monte Carlo Transport Model

To test the viscous decretion disk model, we need to calculate observable quantities (such as flux) for comparison to observations. In principle, the emergent intensity is given by the formal solution to the transfer equation

$$I_\nu^{\rm emerg} = \int_0^{\tau_\nu^{\rm max}} {\rm e}^{-\tau_\nu} S_\nu d_{\tau_\nu} + {\rm e}^{-\tau_\nu^{\rm max}} I_\nu^0 \tag{3.1}$$

where the optical depth is

$$\tau_\nu(z) = -\int_\infty^z \rho \chi_\nu dz \ , \tag{3.2}$$

and the total opacity is given by

$$\chi_\nu = \kappa_\nu + \sigma_\nu \ . \tag{3.3}$$

The source function is expressed by

$$S_\nu = \frac{j_\nu + \sigma_\nu \int R(\nu', \hat{n'}; \nu, \hat{n}) I'_\nu(z, \hat{n'}) d\Omega' d\nu'}{\chi_\nu} \ , \tag{3.4}$$

where j_ν is the emissivity and $R(\nu', \hat{n}'; \nu, \hat{n})$ is the redistribution function which gives the probability of the direction and frequency a photon will be scattered. Unfortunately, the source function depends on knowing the intensity at all points, directions and frequencies.

Since the disk is optically thick, solving the transport equation becomes very complex, and must be solved numerically. Several different numerical techniques have been employed for solving radiation transfer in multiple dimensions including the diffusion approximation, method of discrete ordinates, ray tracing and Monte Carlo (MC) simulations. Although ray tracing techniques are sufficient for simple geometries, such as plane parallel atmospheres, MC is usually the only viable option for complex (3-D) configurations. Furthermore, the relative computational efficiency of MC methods increases with the number of spatial dimensions, frequencies, and with increasing amounts of anisotropy in the radiation field.

3.1 Monte Carlo Algorithm

In order to solve the radiation transfer equation, we employ the code HDUST (see Carciofi & Bjorkman 2006, 2008) which uses MC techniques to simultaneously solve for radiative and statistical equilibrium. The MC code simulates the random (hence the name Monte Carlo) propagation of photons through the medium where they are scattered, absorbed, and reemitted until they eventually leave the interaction region. In doing so, the MC method integrates the transfer equation using a random sampling of the various photon paths (i.e. random ray tracing). This is accomplished by first dividing the total luminosity (from star and disk) into N equal energy monochromatic "photon" packets, each of which has energy

$$E_\gamma = \frac{L\Delta t}{N_\gamma} \ , \tag{3.5}$$

where Δt is the (arbitrarily chosen) simulation time. Each packet has a position($\vec{r}$), direction($\hat{n}$), and frequency(ν'), with the number of photons in the packet $n = E_\gamma/h\nu$. Since the packet contains an ensemble of photons it has a partial polarization described by Stokes parameters, $S = (I, Q, U, V)$.

For each photon packet, the code performs the following sequence of steps:

1. A random location, direction and frequency are selected for photons on the stellar surface. The initial position ($\vec{r}$) on the star is chosen from the probability per area of emitting a photon,

$$\frac{dP}{dA} \propto H(\vec{r}), \tag{3.6}$$

where H is the frequency integrated Eddington Flux as a function of position on the stellar surface. The photon frequency is obtained from the monochromatic flux, H_ν, with probability

$$\frac{dP}{d\nu} \propto H_\nu \ . \tag{3.7}$$

The direction, $\hat{n}$, is chosen from the probability distribution

$$\frac{dP}{d\Omega d\nu} \propto \mu I^*_\nu(\mu) \ , \tag{3.8}$$

where $\mathrm{I}^*_\nu(\mu)$ is the emergent monochromatic stellar intensity as a function of direction $\mu = \hat{n} \cdot \hat{r}$. If the star is rotating, the frequency of the photon is doppler shifted accordingly.

2. Next we calculate the random optical depth. Since the probability that a photon travels an optical depth without an interaction is given by $e^{-\tau_\nu}$, the cumulative probability that the photon will scatter prior to τ_ν is $1 - e^{-\tau_\nu}$. Therefore, $\tau = -\ln \xi$

where ξ is a random number between 0 and 1.

3. Once we have τ_ν we can calculate the distance s that the photon travels to its interaction point. This distance is found by integrating

$$\tau_\nu = \int_0^s \chi_\nu \rho ds \tag{3.9}$$

along the photon path and solving for s. The photon position is then updated to $\vec{r} = \vec{r} + s\hat{n}$, the interaction point.

4. Then we have to determine if the photon is absorbed or scattered. The probability that the photon will be absorbed is

$$a = \frac{\kappa_\nu}{\kappa_\nu + \sigma_\nu} \tag{3.10}$$

with a being the albedo. If $\xi > a$ then the photon packet is absorbed and subsequently reemitted in a new direction and frequency dependant on the local emissivity of the gas, j_ν,

$$\frac{dP}{d\nu d\Omega} \propto j_\nu \ . \tag{3.11}$$

If $\xi < a$ then the photon packet is doppler shifted into the rest frame of the gas, then scattered monochromatically with a probability distribution of

$$\frac{dP}{d\Omega} = \frac{1}{\sigma}\frac{d\sigma}{d\Omega} \tag{3.12}$$

where $\mathrm{d}\sigma/\mathrm{d}\Omega$ is the differential scattering cross section(this determines the new photon direction and polarization). Finally the photon is doppler shifted back into the observer's frame.

5. Steps 2 through 4 are repeated until the photon packet leaves the interaction region (the disk) where they are binned according to frequency and direction.

Typically anywhere from $10^6 - 10^8$ photon packets are used, illustrating the massive amount of CPU time required!

3.2 HDUST

The interaction (i.e., absorption) of the photons with the gas provides a direct sampling of the radiative rates, which ultimately determines the electron temperature. One of the benefits of the MC process is that we can find the location where the individual photon packets are absorbed. In order to conserve energy, once the photon packet is absorbed, is must be reemitted at a different wavelength, never destroyed. Therefore flux is conserved (see Lucy 1999, Bjorkman and Wood 2001), and this procedure automatically solves the radiative equilibrium condition.

To find the NLTE level populations we must solve the the statistical equilibrium equations,

$$n_i \sum_{j \neq i} (R_{ij} + C_{ij}) = \sum_{j \neq i} n_j (R_{ji} + C_{ji}) \tag{3.13}$$

where R_{ij} are the radiative rates(which are sampled from the photon absorptions in the MC simulation) and C_{ij} are the collisional rates between level i and j. Similarly the electron temperature is calculated by balancing the heating rates from photoionization with the cooling rates from recombination (as well as free-free absorption and emission)

$$\int_0^\infty \kappa_\nu (S_\nu - J_\nu) d\nu = 0 \ . \tag{3.14}$$

In order to determine the envelope (disk) structure, HDUST divides the disk into a grid of n_r radial cells, n_μ cells in latitude, and, if desired, n_ϕ cells in the phi direction. Within each cell, the electron temperatures and level populations are assumed to

be constant. Each iteration starts with an initial estimate of the variables (electron temperature, level populations, and density) in each cell. As the MC process is performed, the radiative transition and electron heating rates are sampled in each cell. At the end of the iteration the radiative and heating rates are used to update the level populations and electron temperature, by linearizing eqs. (3.13) and (3.14) and solving for the new level populations and temperature. Finally the disk density and velocities are updated by solving eqs. (2.44-2.46). A new iteration is then started with the updated variables. The simulation proceeds until the variables converge in each cell.

In order to make the run time practical for each iteration, the code requires a parallel-computing system. Parallel-computing systems carry out calculations simultaneously on multiple processors. To run the code in parallel, the photon packets are divided into batches that run independently on each processor. The system consists of a 96-node Beowulf cluster with 1.7 GHz Athlon CPUs.

3.3 Disadvantages to MC

3.3.1 Small Frequency Ranges

One common problem with MC simulations is that the radiation field is typically under-sampled at frequencies where the intensity is low. This problem occurs since the number of photon packets per frequency is proportional to the specific intensity. Therefore, calculating the flux for wavelength ranges of low intensity would require a large total number of photons packets for the simulation. The problem also arises when calculating the emergent flux for a narrow range of frequencies, such as a line profile, where there are few photon packets of that frequency. The solution is to

use a post-processing part of the code, which performs the MC simulation for a specified wavelength range. The technique is also used to obtain good statistics for each individual line transition when sampling the radiative rates that determine the level populations.

3.3.2 Optically Thick Spectral Lines

Although MC techniques work very well for modeling the continuum, problems arise in line formation regions. In these regions the lines may be very optically thick, so it becomes impossible to track the photon packets within these regions. Fortunately the disk is an expanding medium, and we can use the Sobolev approximation to determine the optical depth and photon escape probabilities. In the Sobolev approximation, the line interaction region is assumed to be sufficiently small that the source function and density are constant within the interaction region. Therefore the optical depth and thus the solution to the transfer equation, which normally contain integrations over distance, depend only on the local condition at the point where the interaction occurs. This permits an analytic solution. From the analytic solution one can calculate the escape probability from the Sobolev region as a function of direction,

$$\frac{dP}{d\Omega} = \frac{1 - \mathrm{e}^{-\tau_{\mathrm{sob}}}}{\tau_{\mathrm{sob}}} \quad , \tag{3.15}$$

with τ_{sob} given by

$$\tau_{\mathrm{sob}} = \frac{\pi e^2}{m_e c} f_l \left(\frac{c}{\nu_p}\right) n_l \left(\frac{dv}{ds}\right)^{-1} \tag{3.16}$$

where m_e is the electron mass, f_l is the oscillator strength of the transition, ν_p is the frequency of the photon emitted from the photosphere, and dv/ds is the velocity gradient.

Unfortunately, the Sobolev assumption breaks down along directions with zero velocity gradient, nevertheless, it does produce good estimates of the source function (Hamann 1985). One proposed compromise is to use the Sobolev with Exact Integration (SEI) method developed by Lamers et al. 1987. In the SEI method the source function is determined using the Sobolev approximation, but the emergent intensities are calculated using a full numerical integration of the transfer equation with a line profile function of finite Doppler (or turbulent) width. HDUST uses the SEI method in all line profile calculations.

Chapter 4

Observational Data

One of the reasons that γ Cas was chosen for this project was the wide variety of data available for this star. A thorough search of the literature reveals a wide range of observations across the entire spectrum from X-ray to radio regions. Although not as straightforward to obtain, hydrogen line profiles are also available. Table 4 lists all photometric data that were utilized in constructing the observed SED for γ Cas.

4.1 Observations

4.1.1 Ultraviolet and Visible Observations

UV data was needed in order to determine the effective stellar temperature and radius of γ Cas. Low resolution observations taken using the short-wavelength (1150-2000 Å) and long-wavelength (1850-3300Å) primary cameras with a $10''$ by $20''$ oval entrance aperture were obtained from the International Ultraviolet Explorer (IUE) archive. Data files swp33894.mxlo and lwp13607.mxlo taken July 10, 1988 with a 0.4 second exposure time were utilized. For details about the data reduction see Nichols

Table 4.1: Wavelength and flux of each photometric observation.

Wavelength (μm)	Flux (ergs cm^{-1} s^{-1} μm^{-1})	Source
.44	8.702×10^{-6}	1
.55	4.521×10^{-6}	1
.64	2.288×10^{-6}	1
.90	9.918×10^{-7}	1
1.235	4.79×10^{-7}	2
1.662	1.77×10^{-7}	2
2.159	8.51×10^{-7}	2
12.0	3.08×10^{-10}	3
25.0	3.25×10^{-11}	3
60.0	1.82×10^{-12}	3
800.0	2.34×10^{-16}	4
1100.0	6.94×10^{-17}	4
20000.0	3.45×10^{-21}	5

[1] SIMBAD

[2] 2MASS

[3] Waters et al. (1987)

[4] Waters et al. (1991)

[5] Taylor et al. (1990)

and Linsky (1996). Visible observations consisted of the Johnson B, V, R, and I bandpasses. The magnitudes of the B, V, R, and I bandpasses were obtained from SIMBAD and converted to fluxes using calibration constants consistent with Bessell et al. (1998).

4.1.2 HPOL Visible Spectroscopy and Polarimetry

The visible spectroscopy and polarimetry observations were made using the Halfwave Polarimeter (HPOL) instrument installed on the 36″ telescope at the University of Wisconsin-Madison Pine Bluff Observatory. The instrument provides simultaneous spectrophotometry and spectropolarimetry over a wavelength range of 3200

to 10500 Å. In 1995 HPOL was upgraded to include a 400 X 1200 CCD camera. Prior to this, HPOL covered a wavelength range of 3200 to 7750 Å. Observations prior to 1995 are available online at the MAST archive. For more information about the data reduction and analysis process see Nordsieck & Harris (1996), and Wolff(1996). The observations from HPOL presented in this thesis were taken August 08, 1995.

4.1.3 Infrared Photometry and Spectroscopy

J,H, and K band magnitudes were obtained from the 2MASS archival data. 2MASS consisted of two 1.3m telescopes — one in Mt. Hopkins, Az and one at CTIO, Chile — which were each equipped with a three-channel camera. The camera consisted of a 256 $\times$ 256 array of HgCdTe detectors that were capable of observing the sky simultaneously at 1.25, 1.65, and 2.17 μm (see Skrutskie et al. 2006 for details). Infrared data for the 12, 25, and 60μ wavelengths were taken by the Infrared Astronomical Satellite (IRAS) (Waters et al. 1987). In addition to IRAS, infrared data was also provided by the archives from the Infrared Space Observatory(ISO)(Hony et al. 2000). ISO data was obtained on the medium resolution spectrograph. Millimeter observations of γ Cas were taken for 0.8mm and 1.1mm (Waters et al. 1991). They were obtained with the James Maxwell Telescope using the UKT14 bolometer, with bandwidths (FWHM) of $\Delta(\lambda) = 313$ and 199 μm respectively. The 2 cm observation was taken on the National Radio Astronomy Observatory (NRAO) Very Large Array (VLA) in the 'D' configuration with a synthesized beam width of 5″ (Taylor et al. 1990).

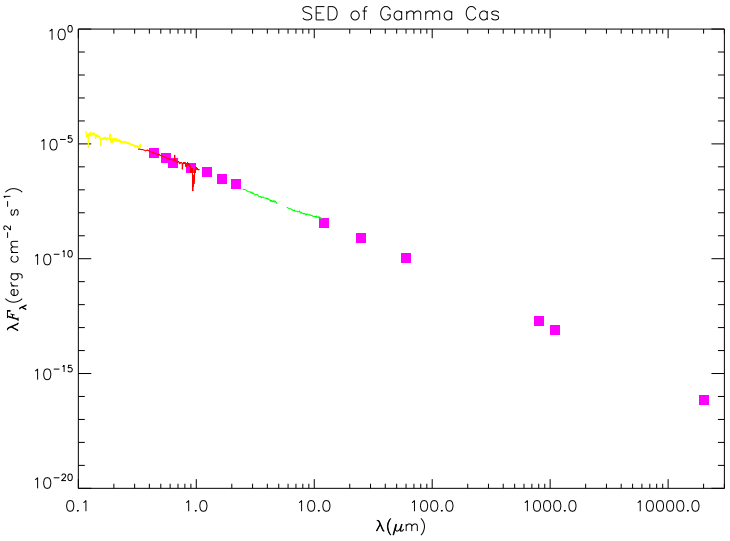

Figure 4-1: SED of γ Cas. The yellow line is UV data from IUE, pink squares are photometric data listed in Table 4, the red line is HPOL data taken in the visible and NIR regions, and the green line is infrared data from ISO.

4.2 Interstellar Reddening and Polarization

Determining a precise value for the interstellar reddening in Be stars is not a trivial matter, due to intrinsic reddening from the circumstellar environment. γ Cas is a relatively close star, so we would expect interstellar reddening to be a small, however these details are important in order for the model to achieve an accurate fit. Using column densities for H I and H_2 in the line of sight to γ Cas, Lowe et al. (1985) derived an upper limit to the color excess, E(B-V) $\leq$ 0.03. Using an E(B-V) of 0.03, and a R_V value of 3.1, the data was dereddened with an IDL program based on the Cardelli,Clayton,and Mathis (1989) parametrization. Figure 4-1 displays the full SED from UV to centimeter.

Although dust grains in the interstellar medium (ISM) are nonspherical, even nonspherical particles cannot polarize light if they are oriented randomly. But in the

ISM, weak magnetic fields can align the grains. Dichroic extinction by aligned grains produces an interstellar polarization component which must be removed from the polarization data. The intrinsic polarization stokes vectors can be expressed as

$$Q_\lambda^* = Q_\lambda^{\rm obs} - Q_\lambda^{\rm ISM} \tag{4.1}$$

$$U_\lambda^* = U_\lambda^{\rm obs} - U_\lambda^{\rm ISM} \tag{4.2}$$

where $\mathrm{Q^{obs}}$ and $\mathrm{U^{obs}}$ are the measured stokes parameters, and $\mathrm{Q^{ISM}}$ and $\mathrm{U^{ISM}}$ are the interstellar polarization components. In terms of the polarization, P_λ, and the position angle, θ, equations (4.1) and (4.2) can be rewritten to be

$$Q_\lambda^* = P_\lambda^{\rm obs}\cos(2\theta^{\rm obs}) - P_\lambda^{\rm ISM}\cos(2\theta^{\rm ISM}) \tag{4.3}$$

$$U_\lambda^* = P_\lambda^{\rm obs}\sin(2\theta^{\rm obs}) - P_\lambda^{\rm ISM}\sin(2\theta^{\rm ISM}) \tag{4.4}$$

In order to determine the intrinsic polarization we must determine $\mathrm{P}_\lambda^{\rm ISM}$ and $\theta^{\rm ISM}$. $\mathrm{P}_\lambda^{\rm ISM}$ can be found using Serkowski's empirical formula(Serkowski et al. 1975) as modified by Wilking, Lebofsky & Rieke (1982). Serkowski's formula requires the wavelength at which the interstellar polarization is the greatest ($\lambda_{\rm max}$) and the magnitude of the polarization at that wavelength. Both of these quantities as well as $\theta^{\rm ISM}$ were adopted from Quirrenbach et al. (1997). Once we have found $\mathrm{P}_\lambda^{\rm ISM}$ the task of determining the total intrinsic polarization is trivial. We can express the total intrinsic polarization as

$$P_\lambda^* = \sqrt{Q^{*2}_\lambda + U^{*2}_\lambda}\ . \tag{4.5}$$

Fig. 4.2 shows the intrinsic polarization of γ Cas. Although electron scattering is wavelength independent, we notice that the intrinsic polarization varies with wavelength, displaying a prominent Balmer jump, a slightly sloping Paschen continuum,

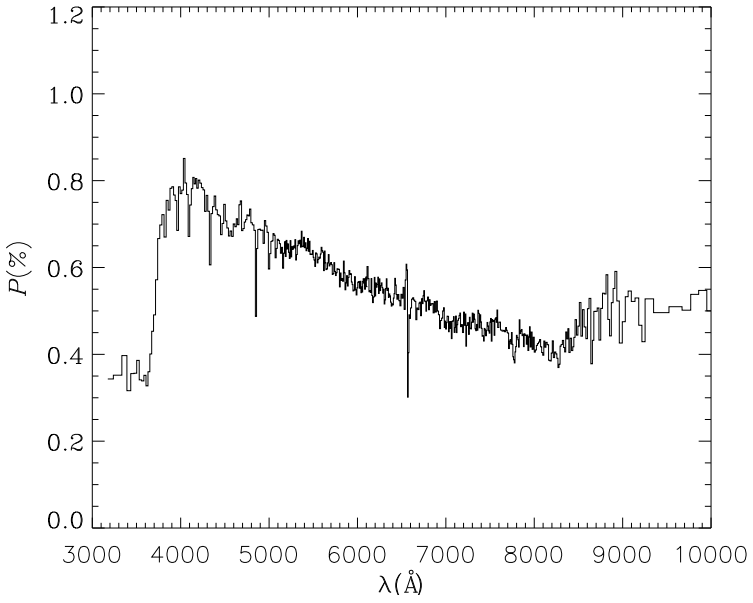

Figure 4-2: Intrinsic Polarization. Polarization percentage after the removal of interstellar polarization.

and a smaller Paschen jump. Such changes in the polarization level as a function of wavelength are attributed to bound-free absorption. In fact, the low levels of polarization shortward of the Balmer and Paschen jump correspond with the maximum value of the hydrogen absorption coefficients.

4.3 Line Profiles

The Hα line profile was obtained using the Ritter Observatory (Toledo, OH) 1 meter telescope using an eschelle spectrograph with a Wright Instruments Ltd. CCD camera. The spectra are divided into 9 orders covering a region of 5285-6600 Å, with a spectral resolving power $R \simeq 26000$. The Hα observation was obtained on September 19, 2004 and was reduced using IRAF based software (see Figure 4-3).

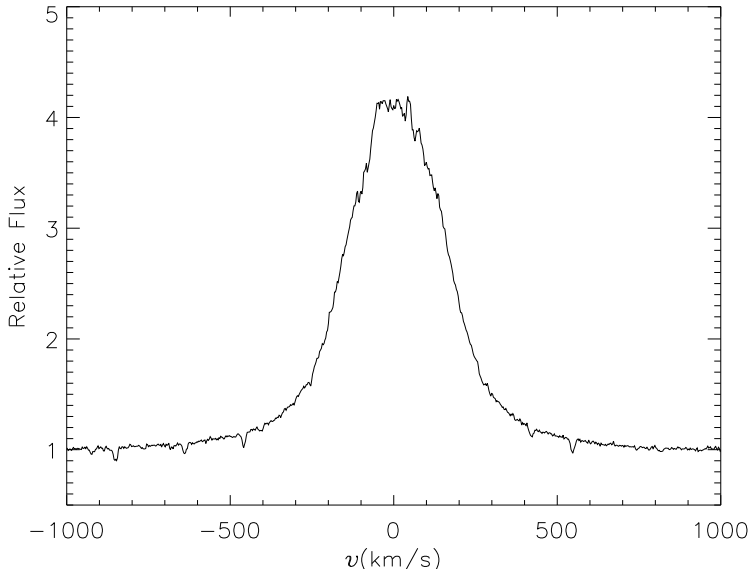

Figure 4-3: Flux normalized Hα line profile.

The IR line profiles (see Fig 4.3) were taken with the SpeX spectrograph on the 3.0m NASA Infrared Telescope Facility(IRTF) on Mauna Kea (Hesselbach, 2009). The IR data was taken February 19, 2007 covering a wavelength range of 0.8 to 2.4 μm. With a 0.3$''$ by 15.0$''$ slit in the short-wavelength cross dispersed observing mode, a resolving power of R$\sim$ 2000 was achieved. The data was reduced using IDL based Spextool software (see Cushing et al. 2004 for further details).

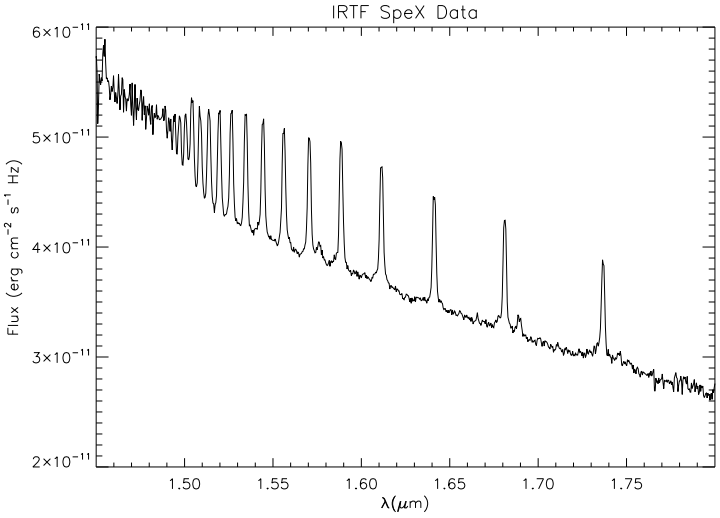

(a) 1.45-1.8 μm

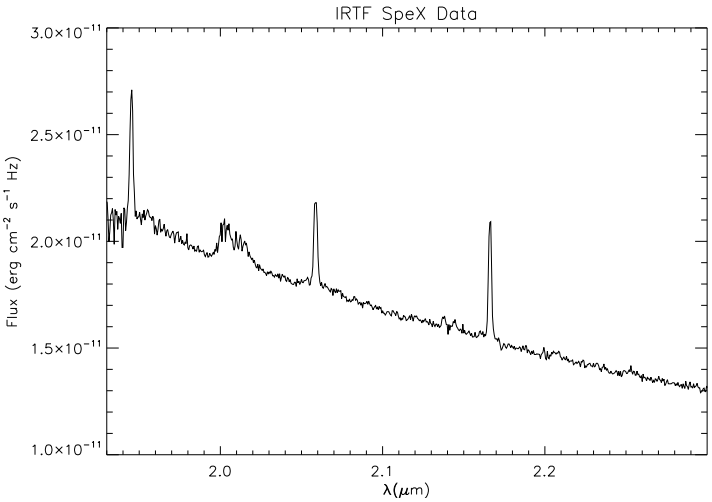

(b) 1.9-2.3 μm

Figure 4-4: IRTF SpeX data. Infrared data taken February 2007 with SpeX for wavelength rages 1.45-1.8 μm, and1.9-2.3 μm.

Chapter 5

Results

In order to test the viscous decretion disk model, it is essential that we minimize the number of free parameters of the model and determine the stellar parameters independently. The effective temperature of γ Cas was determined from fitting a Kurucz model atmosphere with log g of 3.5 to the IUE ultraviolet data. By fitting the UV spectrum, we can obtain the stellar temperature without any excess radiation from the disk which becomes present in the optical due to bound-free emission. The deduced temperature of 25,000 is consistent with the observed spectral type (B0.5 IVe). By fitting the UV spectrum we also found the angular diameter to be .43 mas. Based on the angular diameter, and assuming a stellar radius of 10 $R_\odot$, the required distance of 220 pc to the star was in reasonable agreement with the range of 188 $\pm$ 20 pc denoted in the Hipparcos catalogue(Perryman et al. 1997). From the stellar radius and the effective temperature, the luminosity was found to be 35,000 $L_\odot$ using the relationship

$$L = 4\pi R^2 \sigma T_{\rm eff}^4 \tag{5.1}$$

where σ is Stefan -Boltzmann's constant. A comprehensive search of the literature provided a value of 571 km/s (Collins 1974) for the critical velocity, and 230 km/s

for *vsini* (Slettebak, 1982). Claret's law(2000) is used to describe limb darkening.

For the disk, a grid consisting of 40 cells in the θ-direction (μ cells) and 60 cells in the r-direction was found to produce the best accuracy within reasonable run times. μ cells are spaced in equal steps of density, so that the cell sizes are small near the midplane and become larger with increasing height above the midplane. The disk is terminated in the vertical direction when the density is 10^{-7} times smaller than the density at the midplane. The initial guess for the electron temperature was set to 15000 K, which is roughly 60 percent of $T_{\rm eff}$. Although the initial electron temperature is only a guess and successive numerical iterations determine the true gas temperature, the initial electron temperature determines the grid spacing.

This leaves three free parameters in the model: 1) the mass-loss rate, $\dot{M}$, 2)the disk truncation radius, $R_{\rm d}$, and 3) the inclination, i. Note the disk density, which depends upon the surface density (eqns 2.40 and 2.41), is set primarily by the ratio of $\dot{M}/\alpha$. A value of 0.1 was chosen for α, so that the viscous diffusion timescales roughly agrees with the disk dissipation and creation timescales (Okazaki 2001). Otherwise, if α and $\dot{M}$ are both varied, but the ratio of $\dot{M}/\alpha$ remains constant, the disk density will not change.

The IR excess depends on the density of the disk (Waters 1986), so by treating $\dot{M}$ as a free parameter we can vary the amount of IR excess the model produces.

Similarly, the polarization is strongly dependant on the density of the disk (and $\dot{M}$). We can approximate the polarization of an axisymmetric electron distribution as

$$P \sim \tau_{\rm esc} \gamma \sin^2 i \tag{5.2}$$

Table 5.1: The parameters of the best fitting model for γ Cas.

Parameter	Value
Stellar Parameters	
Spectral Type	B0.5 IVe
R_*	10 $R_\odot$
M_*	17 $M_\odot$
$T_{\rm eff}$	25000 K
log g	3.5
L	35000 $L_\odot$
d	220 pc
$V_{\rm crit}$	571 km s^{-1}
Disk Parameters	
$\dot{M}$	2.0 $\times$ 10^{-11} M$_\odot$ yr^{-1}
α	0.1
ρ_0	1.26 $\times$ 10^{-11} g cm^{-3}
$M_{\rm d}$	4$\times$ 10^{-09} M$_\odot$
$R_{\rm d}$	250 R$_\odot$
$V_{\rm turb}$	36 km s^{-1}
FWHM[1]	3.03 mas
r	0.86
i	30°

[1] FWHM of a gaussian fit to the emergent intensity along the disk's semimajor axis.

where $\tau_{\rm esc}$ is the radial electron scattering optical depth, γ depends on the geometrical shape of the envelope, and i is the inclination (see Brown and McLean 1977). Therefore the polarization not only depends on the density of the disk, but on the inclination as well. In Figure 4.2, the size of the Balmer jump and slope of the Paschen continuum are controlled by the ratio of hydrogen atoms in the $n = 3$ to $n = 2$ states, which is determined by the temperature and the electron density. In the model the size of the Balmer jump and the Paschen slope can be altered by increasing or decreasing $\dot{M}$, while the overall level can be adjusted by changing the inclination angle. Consequently, fitting the model to the polarization data provided the best constraints in determining the inclination.

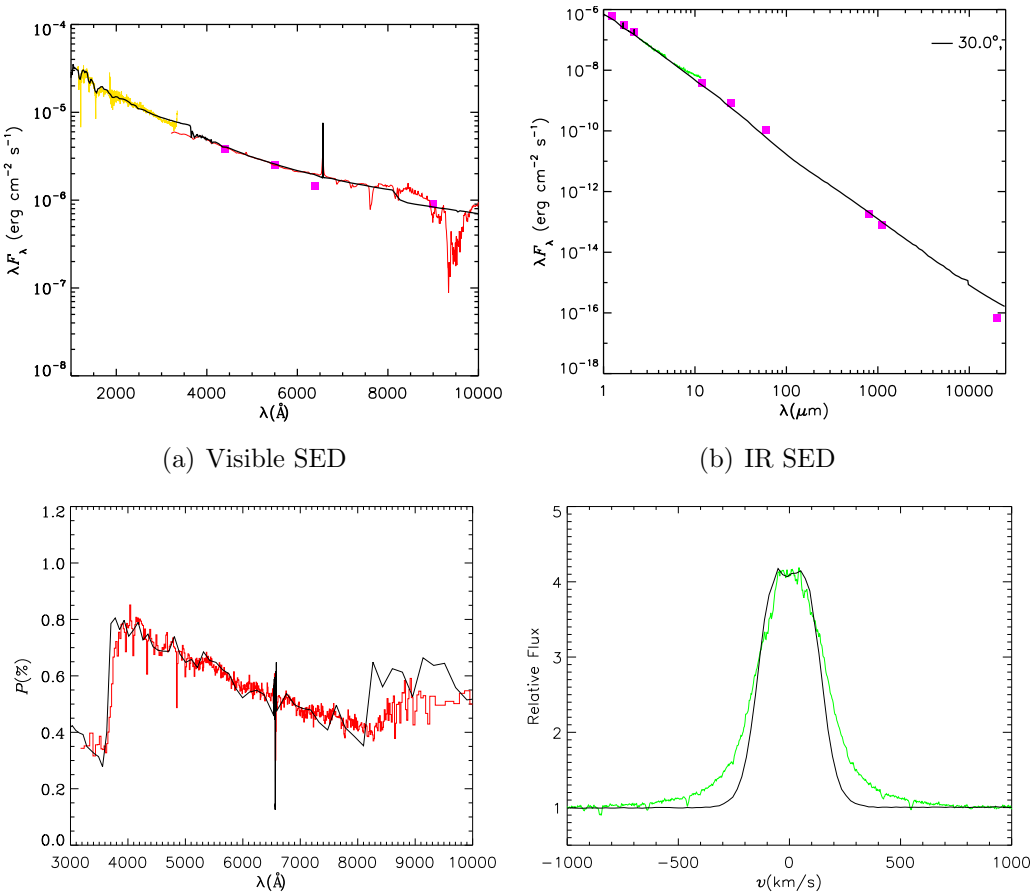

(a) Visible SED

(b) IR SED

(c) Polarization

(d) Hα Line Profile

Figure 5-1: Best fit SED for γ Cas. The upper left panel is the best fit UV and visible SED. In this panel the yellow line is UV data and the red line is HPOL flux. Pink squares represent the B,V,R, and I photometric data. In all cases, the thin black line is the model. The upper right panel displays the IR SED from 1μm - 2 cm. In this panel pink squares are the 2MASS and IRAS data, while the green line is from ISO. The lower left panel displays intrinsic polarization. The red line is the polarization data from HPOL. Finally, in the bottom right panel, the green line is the Hα line profile obtained from Ritter observatory. The flux is normalized to the continuum.

In order to fit the model to the observational data, the code was run using several different R_d values (see chapter 6). First $\dot{M}$ was adjusted until the model fit the visible and IR SED. Then the inclination angle was changed until i fit the polarization data. The best fit is $\dot{M} = 2.0 \times 10^{-11}$ $M_\odot$ yr^{-1}, with a minimum truncation radius R_d = 250 R_*, and $i = 30°$ (see Figure 5). Aside from the UV flux excess shortward of the Balmer jump, the model reproduces the visible and IR SED. Although the predicted IR excess is slightly low for the IRAS bands, the millimeter observations are well reproduced by the model. Similarly the polarization fits very well, with the size of the Balmer jump and Paschen slope in excellent agreement with the model.

The Hα line profile reproduces the correct flux ratio, but is too narrow in the line wings. The line wings may be underestimated by the model since our line profile function is gaussian, and we do not account for the Lorentzian damping wings from pressure broadening.

γ Cas has a wide, single peaked Hα emission line, unlike the classic double-peaked profile. To replicate this single-peaked morphology, we found it necessary to add turbulent broadening to the line profile. We find $v_{\rm turb}$= 36 km/s to best fit the Hα line profile. It is worth noting that fitting the Hα emission strength alone does not independently test the model because the turbulent velocity is a free parameter.

Brackett γ and Brackett 15 line profiles were compared to Spex data, with the Brackett γ line fitting better than the Brackett 15 line. The Brackett lines were calculated using the same turbulent velocity as the Hα line.

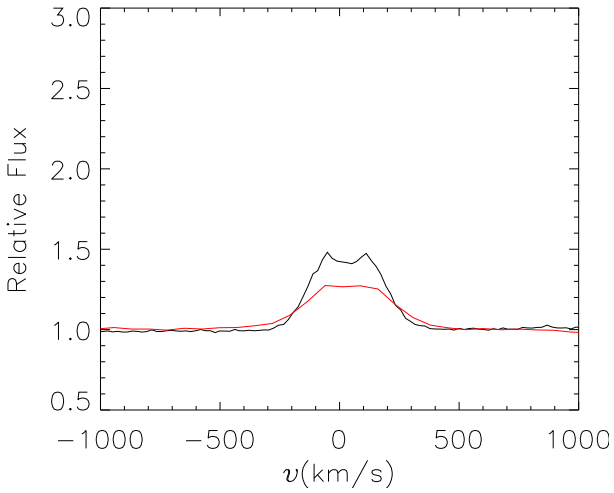

(a) Brackett 15 line profile

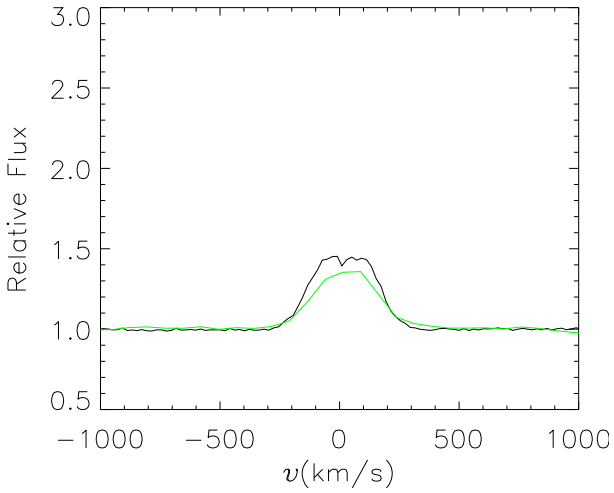

(b) Brackett γ line profile

Figure 5-2: Infrared Line Profiles. Figure 5-2(a) is the Brackett 15 line profile with the black line representing the model and the red line is the SPEX data. Figure 5-2(b) is the SPEX Brackett γ line.

5.1 Temperature Structure

The temperature structure of the disk is shown in Figure 5-3. In this figure, the electron temperature is plotted versus radius for six different latitudes in the disk. The midplane temperature is significantly lower than the disk temperature at high latitudes. In the midplane the temperature drops until it reaches about 7000 K at $\varpi \approx 5$ R_*. The disk temperature then rises steeply, reaching a value of 18000 K before it becomes constant. At higher latitudes the temperature is nearly isothermal with radius averaging about 16,000 K (roughly 60 percent of $T_{\rm eff}$).

This nonisothermal temperature structure is consistent with results for Be star disk models from Carciofi and Bjorkman (2006). They found that the temperature drops like a flat blackbody reprocessing disk (Adams, Lada & Shu 1987), due to the optically thick nature of the inner part of the disk. The temperature reaches a minimum when the disk starts to become optically thin vertically. As the disk becomes optically thin, ionizing photons are able to reach the lower latitudes of the disk. This allows the disk temperature to heat up to the optically thin radiative equilibrium temperature at larger radii.

HDUST calculates the disk temperature for a pure hydrogen disk, however, metals can cool the gas due to the escape of collisionally excited line radiation or heat the gas by the process of photoionization. Models produced by Sigut and Jones (2007), suggest that for the high density disk of γ Cas, metals add both heating and cooling, with the net result that the disk temperature remains similar to a pure hydrogen disk. Sigut and Jones (2007) also find that the temperature along the midplane reaches a minimum between 5 and 10 R_*, then rises to become isothermal at outer radii and

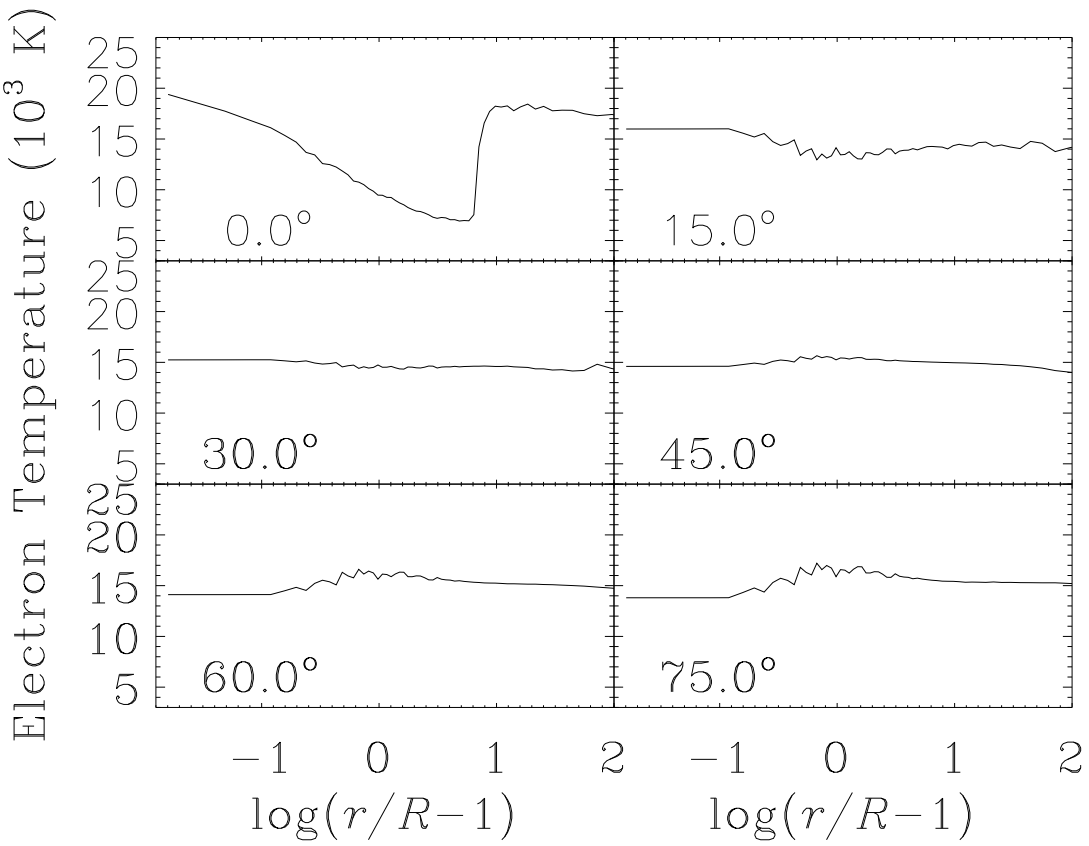

Figure 5-3: Temperature Structure of the Disk. Plot of the electron temperature as a function of radius (with R the stellar radius and r the disk radius), for six different latitudes within the disk.

that the upper latitudes of the disk are isothermal. Unfortunately, due to the many differences in the methods used by both models, it is only possible to compare the disk temperature structures qualitatively, but we do find that overall the Sigut and Jones temperature structure is reproduced by HDUST.

5.2 Density and Level Populations

The model HDUST used a 25 level hydrogen atom with the first 12 levels being explicit NLTE levels, while the upper 13 levels are implicit levels assumed to have LTE populations. Figure 5.2 displays the n=1, 2, and 3 level populations (n_i/N_h) number for each state versus radius. The majority of the hydrogen is ionized, even in the midplane. Of interest is the sharp drop in the level population for n_1 at $r \sim 5$. This is the same location where the disk temperature reaches a minimum, implying that the disk becomes optically thin to ionizing radiation at this point.

From Figure 5-5 it is evident that γ Cas has a relatively dense disk since excess flux due to bound-free emission begins in the optical region. The midplane number density of hydrogen atoms is 1.25×10^{13} cm^{-3} at the base of the midplane. Figure 5.2 plots the number density versus radius for the midplane, which decreases rapidly with radius $\rho \sim r^{-3.7}$. From the number density we can find ρ_0, which is the mass density at the base of the midplane. The value of 1.26×10^{-11} g/cm^3 which is typical for a dense disk, falls within the density range of 1-3 $\times 10^{-11}$ g/cm^3 for type B0-B3 stars modeled by Waters, Coté, & Lamers (87). However, their model produced a power-law fit of $\rho \sim r^{-3.25}$ for the IR excess of γ Cas (see introduction). Hony et al.

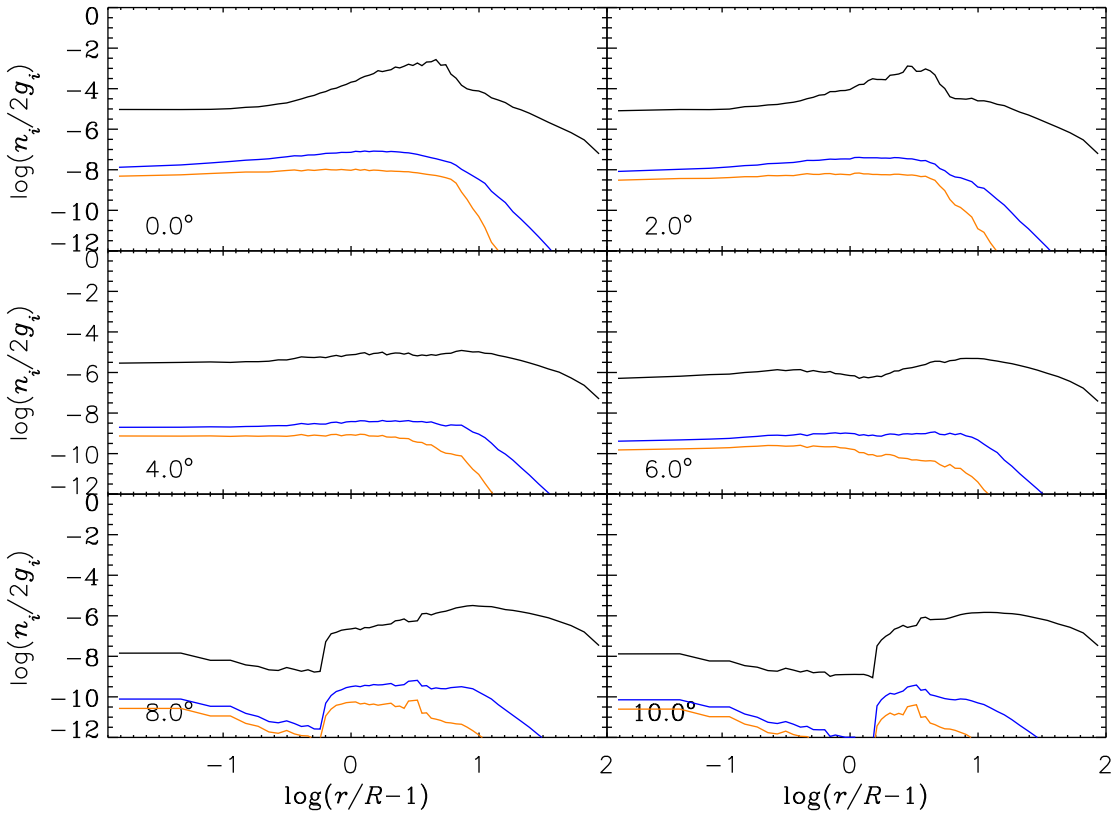

Figure 5-4: Hydrogen Level Populations. The first 3 hydrogen level populations as a function of radius. The n= 1 level is black, the n= 2 level is blue, and the n =3 level is orange.

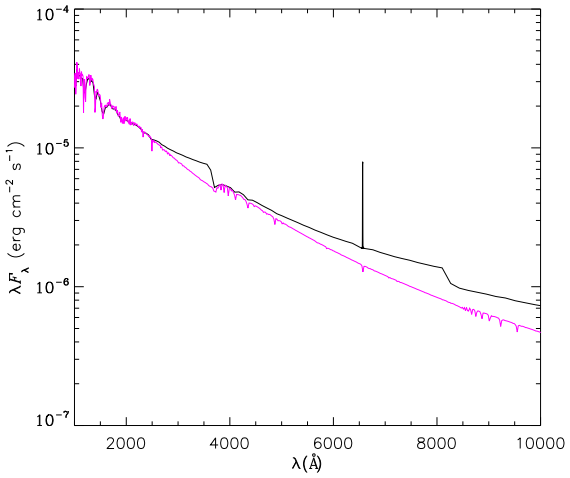

(a) 1000-10000 Å

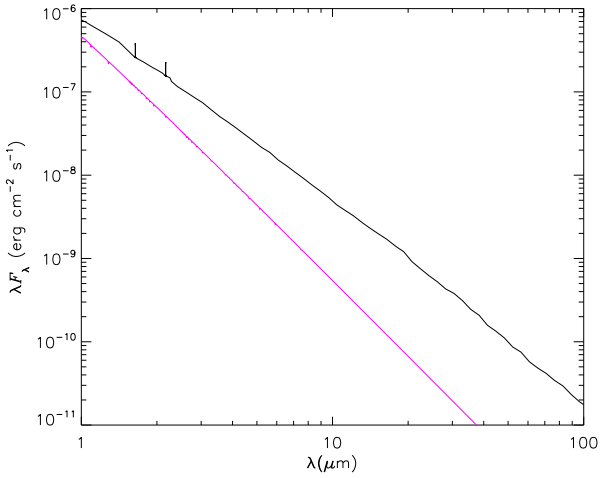

(b) 1-100 μm

Figure 5-5: The two figures demonstrate the amount of excess flux due to the circumstellar material. Figure 5-5(a) is the UV and visible SED with the black line representing the model, and the pink line is the Kurucz model for an effective temperature of 25000 K and log g of 3.5. Figure 5-5(b) displays the IR excess from 1 to 100 μm.

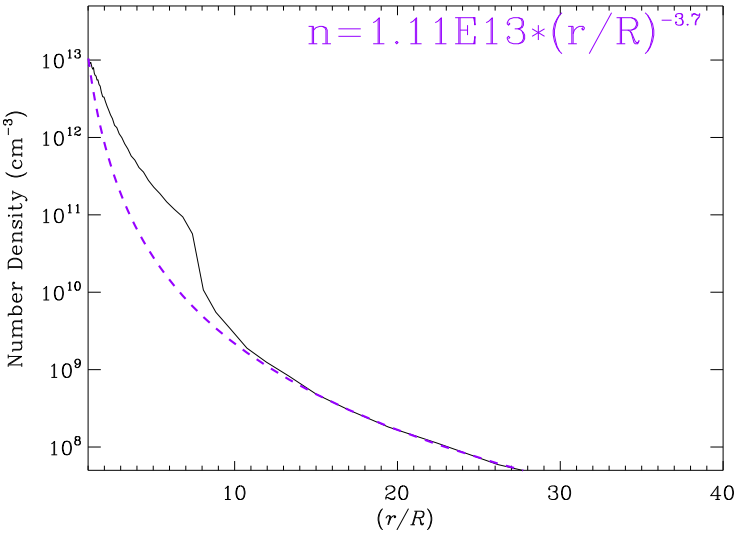

Figure 5-6: The midplane hydrogen number density(cm^{-3}) as a function of radius. Shown for comparison is a power-law fit of the form $n = n_0 * (r/R_*)^{-n}$ (dashed purple line). The power-fit was performed for large r, since the larger radii are mainly responsible for the IR excess.

(2000) derive ρ_0 of 3×10^{-11} g/cm^3 by fitting a simple power law distribution to ISO data. Finally, Jones & Sigut (2007) obtain values of $\rho \sim (3 - 5 \times 10^{-11})(r/R_*)^{-2.5}$ g/cm^3 for the density of the disk based on their best fit to the average disk temperature and energy loss in Hα of γ Cas (although when they use their model to fit ISO data, they find $\rho_0 = 1 \times 10^{-11}$ g/cm^3).

By summing over all cells in the grid, we derive the mass of the disk to be 4×10^{-9} M$_\odot$. If we have an $\dot{M}$ of 2×10^{-11} M$_\odot$ yr^{-1} then it would take 200 years to form such a disk. In the viscous decretion scenario we assume that mass is added from some source such as nonradial pulsations of explosive "events". According to Doazan et al. (1984), γ Cas has only been in the emission phase since the mid-1940's, it seems that this alone would not add enough mass to form the disk, unless $\dot{M}$ is larger. If $\alpha = 0.3$, then $\dot{M}$ would be $6 \times 10^{-11} M_\odot \mathrm{yr}^{-1}$, and it would take only take 70 years for the disk to form. So perhaps α should be larger.

5.3 Images

HDUST has the ability to produce high resolution images of the emergent intensity. Although such resolution is well above the capabilities of ground and space based telescopes, images can be used to produce synthetic visibilities for comparison to optical interferometry observations. Figure 5-7 provides images of the Hα and Brackett 15 line profile regions within the disk. The image resolution is 10 solar radii per pixel. In Hα the two horizontal black bands across the stellar image are very apparent. There is no physical reason to suggest that low intensity regions exist in bands within the disk so they may be artifacts of the grid cell structure. In the Hα region there is a sharp drop in intensity at about 5 stellar radii, which is the location where the line emission becomes optically thin. Since the opacity for Brackett 15

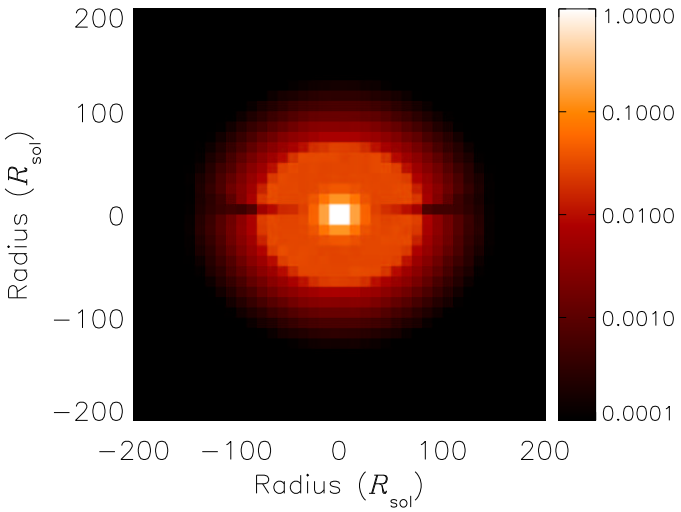

(a) Hα

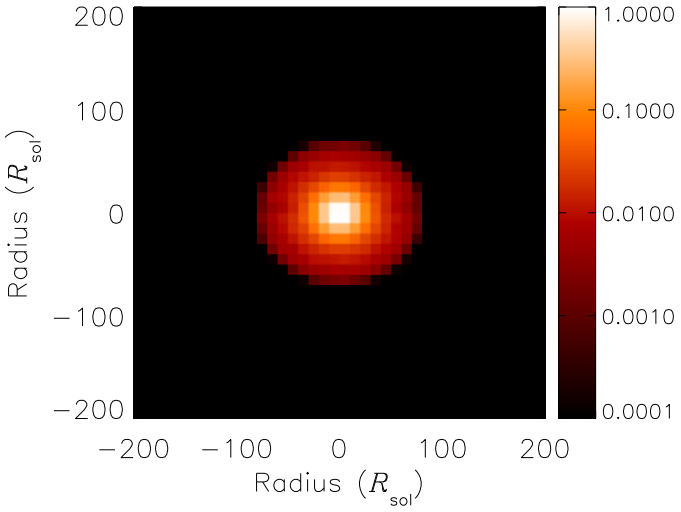

(b) Brackett 15

Figure 5-7: Images of Hα and Brackett 15 lines. The image on the left is a map of intensity as a function of radius for Hα and the intensity map of the right is for the Brackett 15 line.

is less than for Hα, the size of the Brackett 15 emitting is smaller than the Hα region. Consequently, the Brackett 15 line probes conditions in the inner disk.

Figure 5-8 provides a series of images (channel maps) across the Hα line profile. Each image is centered at a different doppler shift, as indicated. The emitting area increases as we move from the continuum (a) towards the peak emission (c). The emitting region increases since we are picking up low velocity material at larger radii in the disk. Then the emission decreases until line center (d), which would be the central reversal if we had a double-peaked line profile. The total emitting area then increases back to its maximum at (e), where it drops off again as we move back towards the continuum. Another area where these images can be useful is for spectroastrometry techniques. In particular, the location of the photocenter versus wavelength can be used to determine if material in the disk is rotating with Keplerian velocity($v_\phi \propto \varpi^{-1/2}$), or angular momentum conserving rotation ($v_\phi \propto \varpi^{-1}$).

Currently, optical and IR interferometry are capable of determining the angular sizes of emitting regions and the apparent ellipticity of the isopotes. By modeling visibilities obtained from interferometric observations, Tycner et al. (2006) demonstrated that a gaussian intensity distribution was a better fit to the disk structure than either a uniform disk or ringlike structure. If the intensity function of the central star is treated as a separate circularly symmetric uniform disk brightness, they are able to determine the semimajor axis (the full width at half maximum, FWHM, of the gaussian).

By fitting the intensity as a function of radius for our images, along a cross cut of the disk in the x and y directions, to a gaussian function, we can determine the model's semimajor and semiminor axes. In the post processing phase of HDUST, the specified

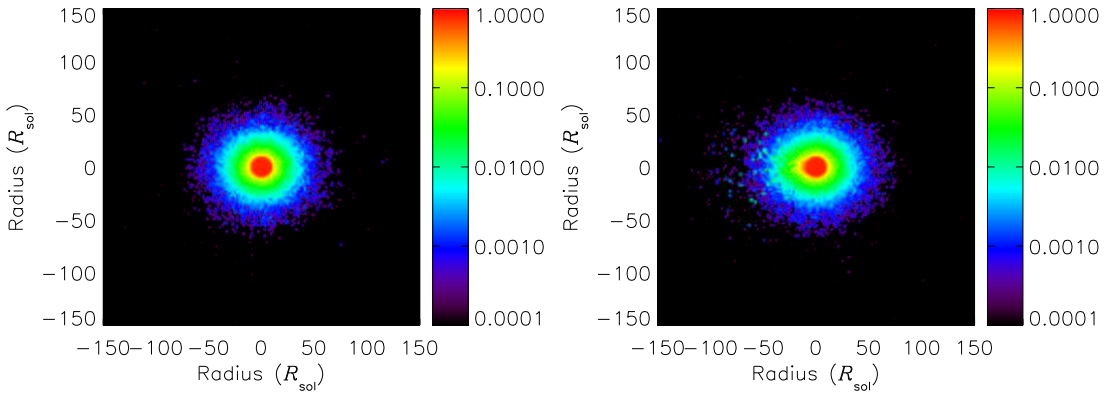

(a) Continuum

(b) v = -280 km s^{-1}

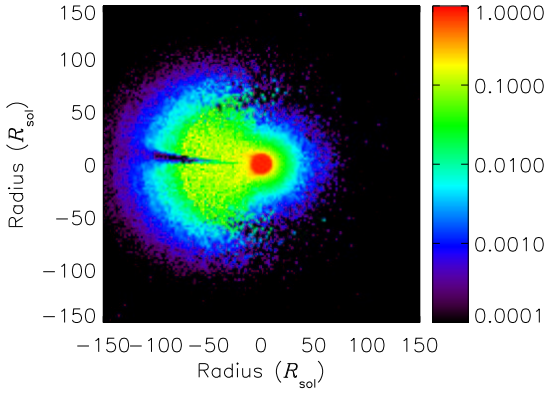

(c) v= - 142 km s^{-1}

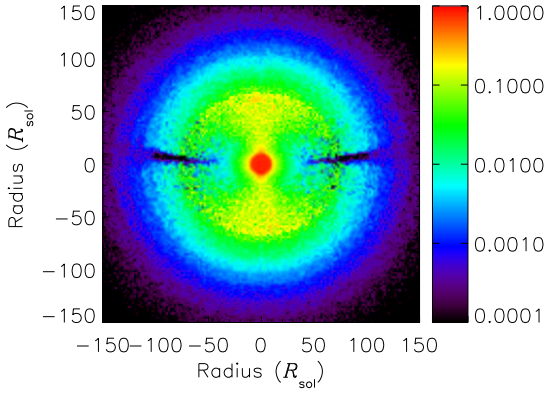

(d) v= 0 km s^{-1}

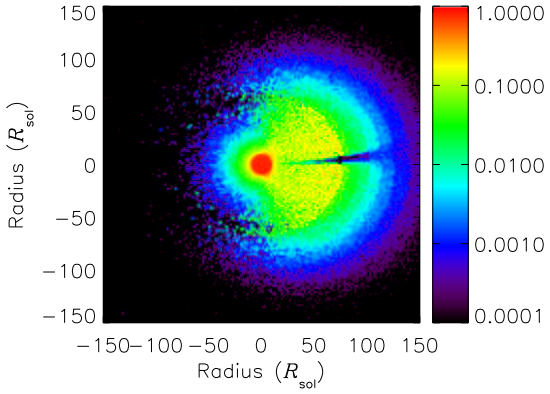

(e) v = 142 km s^{-1}

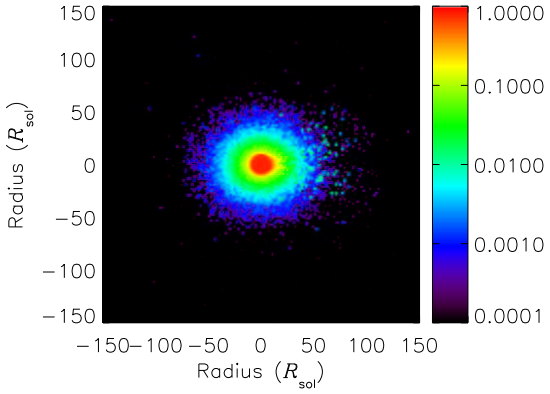

(f) v = 280 km s^{-1}

Figure 5-8: Channel maps of the Hα emission line

wavelength regions for Hα and for the K-band were set to be the same as the Hα and K-band filters used for the interferometric data. To remove the stellar contribution to the intensity, we removed pixels between -10 and 10 solar radii. Although this technique is not quite the same as that applied by Tycner et al. (2006), it allows us to estimate the semimajor and semiminor axes without the large intensity peak from the central star .

For the best fit model we find a semimajor axis size of 3.01 $\pm$ 0.03 mas and a semiminor axis of 2.61 $\pm$ 0.01 mas for the Hα region. Their ratio $r = 0.864 \pm 0.005$ which agrees with our inclination angle of 30 degrees ($\cos i = r$). The K-band semimajor axis from our model is 1.20 $\pm$ 0.04 mas with a $r = 0.83 \pm 0.01$ which again gives us an inclination of 30 degrees.

Chapter 6

Discussion

For the most part, the viscous decretion model well reproduces the entire SED from the near UV to radio, as well as the polarization, Hα, and Brackett γ line profiles. One noticeable discrepancy is the excess flux just shortward of the Balmer jump (see Fig. 5). This could possibly be the result of not including gravity darkening. Including gravity darkening will increase the stellar photospheric Balmer jump which will offset the filling in by disk emission. Similarly there is a mismatch longward of the Paschen jump, which could be a consequence of the fact that the code does not include all of the broadening mechanisms where the lines converge near the series limit. The wings of the line profile also are narrower than the observed spectra. Again, this may be the result of not properly including collisional broadening or some other broadening mechanism, such as scattering off the hot thermal electrons.

The mm observations fit the slope of the model, although the predicted flux is too high for the centimeter photometric band (see Figure 5). Millimeter and centimeter observations probe the outer regions of the circumstellar disk. This is of particular importance since our SED was fit with the disk truncation radius R_d being a free

parameter. However, there is some evidence that γ Cas may have a binary companion (Harmenec et al. 2000, Miroshnichenko et al. 2002). In binary systems, it is possible that the companion can truncate the primary's disk. Using the proposed period (204 days) and mass (.5 $R_\odot$) of the companion from Harmanec (2000) and Miroshnichenko (2002), and adopting an inclination angle $i = 55$ degrees, the semimajor axis, $a =$ 1.45AU. This gives the primary's Roche radius,

$$R_{\rm roche} = a\frac{0.49q^{-2/3}}{0.6q^{-2/3} + \ln(1 + q^{-1/3})} = 200R_\odot \ , \tag{6.1}$$

where q is the ratio of the companion's mass to the primary's mass Eggleton (1983). Therefore we have a binary truncation radius, $R_d = 20\ R_*$.

To explore the possibility that the disk is truncated we compared the 20 R_* to a 100 R_* and 250 R_* truncation radius (see Fig. 6-1). Note that the visible SED is insensitive to increasing R_d as long as $\dot{M}$ is decreased so that the surface density remains constant. Not only does the 250 R_* truncation radius model fit have the greatest flux in the far IR, but it also fits the mm observations the best. At larger wavelengths the opacity increases giving the disk a larger effective radius which leads to a greater IR excess at that wavelength. Therefore the mm and cm observations should provide the best indication of the size of the disk and thereby rule out disk truncation by a binary.

Although there is growing evidence that γ Cas may be a binary system, the presence of a companion is still tentative. Furthermore, a binary companion may not truncate the disk. The disk has been in the rebuilding phase since the mid-1940's. Using equation (2.26) where $t_{\rm diff}$ is 70 years, with $a = 16$ km s^{-1} we find that γ Cas would have an outer disk radius equal to our disk truncation radius if $\alpha = 0.3$.

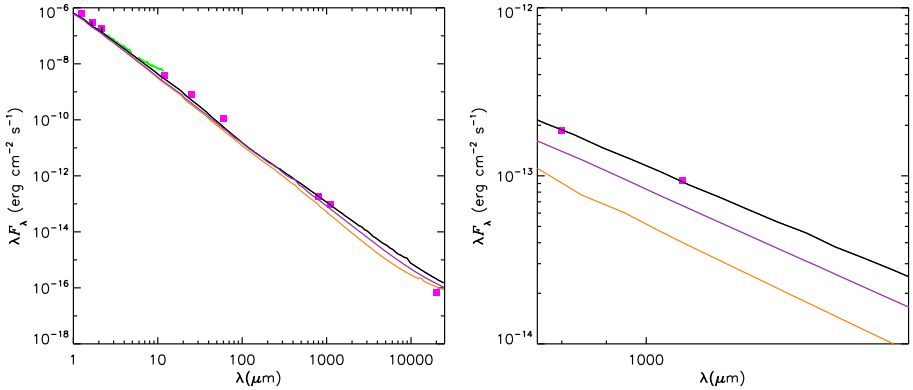

(a) IR to centimeter SED (b) MM

Figure 6-1: Disk truncation radii. Figure 6-1(a) displays the IR SED for the 20 R_* (orange line), 100R_* (purple line), and the 250 R_* (black line) truncation radii. The 250 R_* truncation radius has a greater IR excess and fits the mm observations the best. The model overproduces the cm flux for all three truncation radii. Figure 6-1(b) is a closeup of the mm region.

The largest discrepancy between our model and observations is the interferometry results, where our value for r is significantly larger than observed. Since r is determined by the inclination value, the interferometry results constrain the inclination angle of the disk. Table 6.1 list the models parameters for γ Cas compared to several recent interferometry studies in the Hα and K bands. The size of the disk (FWHM) is relatively close to the observed values. The size of the semimajor axis for the Hα region is 15 percent smaller than the interferometric observations and the K band fit is 8 percent smaller than the CHARA K band observations.

Although r is more consistent with older interferometry values, newer observations place the inclination higher. Tycner et al. (2006) attribute their higher inclination angles to a larger range of baseline projection angles on the plane of the sky. A larger range of baseline projection angles should in principle provide a better measure of r and hence a better indication of the inclination. But unfortunately Our fit is

Table 6.1: Comparisons between this work and published data for the interferometry of γ Cas.

inclination deg	FWHM mas	r	source
	Hα Band		
30	3.01 ± .03	0.864 ± .005	1
46	3.47 ± 0.025	0.70 ± 0.02	2
38	3.67 ± 0.09	0.79 ± 0.3	3
55	3.59 ± 0.04	0.58 ± 0.03	4
	K band		
30	1.21 ± .04	0.862 ± .003	1
51± 4	1.35	0.59 ± 0.03	5

[1] This work

[2] Quirrenbach et al. (97)

[3] Tycner et al. (03)

[4] Tycner et al. (06)

[5] Gies et al. (07)

inconsistent with the later interferometry data. Our values for r are a consequence of the low inclination of the model ($r \approx \cos i$).

In the model fit, the polarization data was the major constraint for the inclination. If we instead fix $i = 55°$ and fit the SED, then the model predicts polarization percentage values that are much too high(see Figure 6-2).

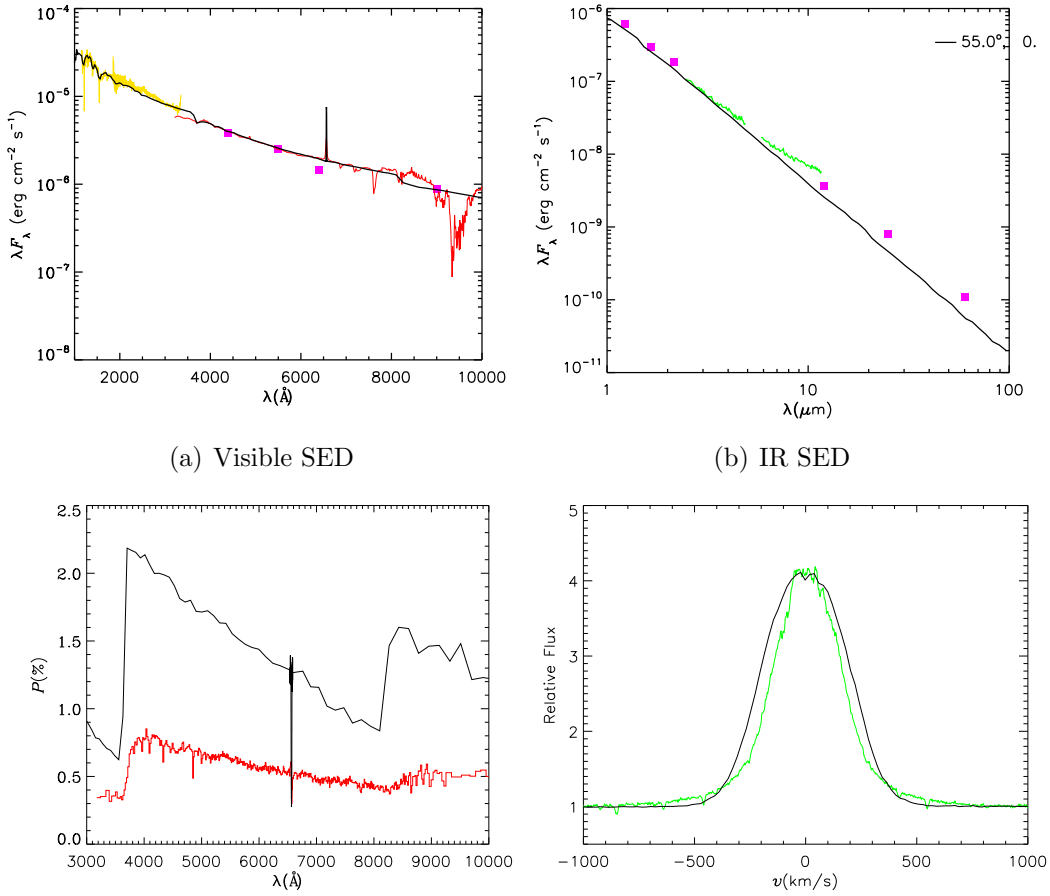

(a) Visible SED

(b) IR SED

(c) Polarization

(d) Hα Line Profile

Figure 6-2: Model results for fixed inclination of 55 degrees. The SED was fit while holding the inclination constant. The model overestimates the polarization by at least a factor of 2.

Both the polarization and Brackett 15 line originate in the inner disk, while Hα and Brackett γ are formed over a much larger region. Both Hα and Brackett γ emission line strength (equivalent width) are well fit by the model, but the Brackett 15 line is overproduced. This in combination with the polarization being too large points to some discrepancy in the inner disk region. There may be some physical reason the model does not reproduce the conditions in the inner disk, or it could be a peculiarity in this Be star. For example, γ Cas displays unusually hard x-ray emission, which might be attributed to a possible white dwarf companion or, as Robinson, Smith,& Henry (2002) propose, a magnetic dynamo located within the inner part of the circumstellar disk. Regardless of the physical origin any additional heating of the inner disk will increase its scale height and lower the density, thereby reducing the Brackett 15 emission and possibly the polarization.

One other factor that we did not include is gravity darkening. In a rapidly rotating star, the temperature gradient is shallower in the equator than near the poles, so the effective temperature is less at the equator than at the poles. In a star rotating close to critical velocity, the polar flux is significantly brighter and hotter than the equatorial flux. These changes in ionizing flux will alter the ionization fraction and disk temperature, which will influence the SED or polarization values calculated by the model.

Chapter 7

Conclusion

Regardless of the physical mechanism initially responsible for disk formation, viscosity will cause orbiting material to diffuse outward. Therefore it is possible to model the steady-state circumstellar disk as a viscous decretion disk. To model the viscous decretion disk we have employed the code HDUST, which calculates the temperature structure of the disk, solves the steady state fluid equations, and finally calculates the observable properties. By comparing observational properties of γ Cas (a well studied Be star), to those predicted by our model, we are able to first critically test the viscous decretion scenario, and then determine the physical parameters of the disk.

We conclude that the viscous disk scenario is generally consistent with the observational data. We were able to model the star with only three free parameters, $\dot{M}$, disk truncation radius, and inclination which were found to be $\dot{M} = 2.0 \times 10^{-11}$, the minimum truncation radius $R_d = 250\ R_*$, and $i = 30$ degrees. Overall the visible SED and polarization data fit the Balmer jump well, indicating that we have correctly determined the density and the $n = 3$ to 2 level populations. The Hα line

profile predicts the correct relative flux although the line wings are too narrow, while in the infrared the Brackett γ line profile better predicts the observed relative flux than the Brackett 15 line.

However, one area of concern is the low inclination angle. Recent interferometric observations place the inclination angle at 55 degrees. When the inclination angle was held fixed at 55 degrees, and the SED was fit, the model greatly overestimated the polarization. Such inaccuracies in the polarization value and the discrepancy in the Brackett 15 line fit may suggest problems with the inner disk as both are formed in this region. However, before reaching this conclusion, we must first investigate the effects of gravity darkening. If the indirect effect of gravity darkening does not significantly raise the inclination angle, then attention should be directed towards the inner disk. In the future, once the model successfully replicates observable data, we can begin to investigate the process of disk loss and formation, as well as the density waves in the disk thought to be responsible for the V/R variations.

References

Adams, F. C., Lada, C. J., & Shu, F. H. 1987, ApJ, 312, 788

Bessell, M. S., Castelli, E. & Piez, B. 1998, A & A , 333, 231

Bjorkman, J. E., & Cassinelli, J. P. 1993, ApJ, 409, 429

Bjorkman, J. E. 1997, in Stellar Atmospheres: Theory and Observations, ed. J. P. de Greve, R. Blomme, & H. Hensberge (New York: Springer), 239

Bjorkman, J. E., & Wood, K. 2001, ApJ, 554, 615

Brown, J. C., & McLean, I. S. 1977, A&A, 57, 141

Brown, J. C., Telfer, D., Li, Q., Hanuschik, R., Cassinelli, J. P., & Kholtygin, A. 2004, MNRAS, 352, 1061

Carciofi, A. C., & Bjorkman, J. E. 2006, ApJ, 639, 1081

Carciofi, A. C., & Bjorkman, J. E. 2008, ApJ, 684, 1374

Carciofi, A. C., Okazaki, A. T., le Bouquin, J-B., Stefl, S. Rivinius, Th., Baade, D., Bjorkman, J. E., & Hummel, C. A. 2009, A&A, 504, 915

Cardelli, J. A., Clayton, G. C., & Mathis, J. S. 1989, ApJ, 345, 245

Cassinelli, J. P., & Hartmann, L. 1977, ApJ, 212, 488

Cassinelli, J. P., Brown, J. C., Maheswaran, M., Miller, N. A., & Telfer, D. C. 2002, ApJ, 578, 951

Chokshi, A., & Cohen, M. 1987, AJ, 94, 123

Claret, A. 2000, A&A, 363, 1081

Collins, G. W. 1974, ApJ, 191, 157

Collins, G. W. 1987, "Physics of Be Stars" in IAU Colloq. 92, Physics of Be Stars, ed. A. Slettebak & T. P. Snow (Cambridge: Cambridge Univ. Press), 3

Cranmer, S. R. 2005, ApJ, 634, 585

Cushing, M. C., Vacca, W. D., & Rayner, J. T. 2004, PASP, 116, 362

Donati, J. -F., Wade, G. A., Babel, J., Henrichs, H. F., de Jong, J. A., & Harries, T. J. 2001, MNRAS, 326, 1265

Doazan, V., Franco, M., Ruskoni, L., Sedmak, G., & Stalio, R. 1984, A&AS, 55, 1

Eggleton, P. P. 1983 ApJ, 268, 368

Gies, D. R. et al 2007, ApJ, 654, 527

Hamann, W.-R. 1985, A&A, 148, 364

Harmanec, P., et al. 2000 A&A, 364, L85

Henrichs, H. F., et al. 2000 in Smith, M. A., Henrichs H. F., Fabregat, J., eds, ASP Conf. Ser. Vol. 214, The Be Phenomenon in Early-Type Stars. Astron. Soc. Pac. San Francisco, p 324

Hesselbach, E. N. Ph. D. thesis, University of Toledo

Hony, S. et al. 2000, A&A, 355, 187

Hummel, W., & Hanuschik, R. W. 1997, A&A, 320, 852

Kroll, P., & Hanuschik, R. W. 1997 in IAU Colloq. 163, Accretion Phenomena and Related Outflows ed D. T. Wickramasinghe, G. V. Bicknell, & L. Ferrario(ASP Conf. Ser. 121; San Francisco:ASP), 494

Lamers, H. J. G. L. M., Cerruti-Sola, M., & Perinotto, M 1987, ApJ, 314, 726

Lee, U., Osaki, Y., & Saio, H. 1991, MNRAS, 250, 432

Lopes de Oliveira, R., Motch, C., Smith, M. A., Negueruela, I., & Torrejón, J. M. 2007, A&A, 474, 983

Lowe, R. P., Moorhead, J. M., Wehlau, W. H., Barker, P. K., & Marlborough, J. M. 1985, ApJ, 290, 325

Lucy, L. B. 1999, A&A, 344, 282

Millar, C. E., & Marlborough, J. M. 1998 ApJ, 494, 715

Millar, C. E. & Marlborough, J. M. 1999 ApJ, 526, 400

Miroshnichenko, A. S. Bjorkman, K. S. & Krugov, V. 2002, PASP, 114, 1226

Nichols, J. S., & Linsky, J. L. 1996, AJ, 111, 517

Nordsieck, K., & Harris, W. 1996, in Astronomical Society of the Pacific Conference Series, Vol. 97, Polarimetry of the interstellar medium, ed. W. G. Roberge & D. C. B. Whittet, 100

Okazaki, A. T. 1991, PASJ, 43, 75

Okazaki, A. T. 2001, PASJ, 53, 119

Owocki, S. P., & ud Doula, A. 2003, in ASP Conf. Ser. 305, Magnetic Fields in O, B, and A Stars: Origin and Connection to Pulsation, Rotation, and Mass Loss, ed. L. A. Balona, H. F. Henrichs, & R. Medupe (San Francisco: ASP), in press

Perryman, M. A. C. et al. 1997, A&A, 323, L29

Poeckert, R., & Marlborough, J. M. 1978, ApJ, 220, 940

Porter, J. M. 1996, MNRAS, 280, 31

Porter, J. M. 1997, A&A, 324, 597

Porter, J. M., & Rivinius, T. 2003, PASP, 115, 1153

Quirrenbach, A., Buscher, D. F., Mozurkewich, D., Hummel, C. A., & Armstrong, J. T. 1994, A&A, 283, L13

Quirrenbach, A., et al. 1997, ApJ, 479, 477

Rivinius, Th., Baade, D., Štefl, S., Stahl, O., Wolf, B., & Kaufer, A. 1998, A&A, 333, 125

Rivinius, Th., Baade, D., & Štefl, S. 2003, 411, 229

Robinson, R. D., Smith, M. A., & Henry, G. W. 2002, ApJ, 575, 435

Serkowski, K., Mathewson, D. S., & Ford, V. L. 1975, ApJ, 196, 261

Shakura, N. I., & Sunyaev, R. A., 1973, A&A, 24, 337

Sigut, T. A. A., & Jones, C. E. 2007, ApJ, 668, 481

Skrutskie, M. F., et al. 2006, AJ, 131, 1163

Slettebak, A. 1982, ApJS, 50, 55

Smith, M. A., Cohen, D. H., Gu, M. F., Robinson, R. D., Evans, N. R., & Schran, P. G. 2004, ApJ, 600, 972

Snow, T. P., Jr. 1981, ApJ, 251, 139

Stee, P., et al. 1995, A&A, 300, 219

Stoeckley, T. R. 1968, MNRAS, 140, 141

Struve, O. 1931, ApJ, 73, 94

Taylor, A. R., Dougherty, S. M., Waters, L. B. F. M., & Bjorkman, K. S. 1990, A&A, 231, 453

Telting, J. H., Waters, L. B. F. M., Persi, P., & Dunlop, S. R. 1993, A&A, 270, 355

Townsend, R. H. D., Owocki, S. P., & Howarth, I. D. 2004, MNRAS, 350, 189

Tycner, C., et al. 2004, AJ, 127, 1194

Tycner, C., et. al. 2006, AJ, 131, 2710

Waters, L. B. F. M. 1986 A&A, 162, 121

Waters, L. B. F. M., Boland, W., Taylor, A. R., van de Stadt, H., & Lamers, H. J. G. L. M. 1989, A&A, 213, 19

Waters, L. B. F. M., Marlborough, J. M., van der Veen, W. E. C., Taylor, A. R., & Dougherty, S. M. 1991, A&A, 244, 120

Wilking, B. A., Lebofsky, M. J., & Rieke, G. H. 1982, AJ, 87, 695

Wolff, M. J., Nordsieck, K. H., & Nook, M. A. 1996, AJ, 111, 856

Wood, K., Bjorkman, K. S., & Bjorkman, J. E. 1997, ApJ, 477, 926